CD300a immunoreceptor regulates ischemic tissue damage and adverse remodeling in the mouse heart and kidney

Nanako Nishiyama[1,2,*], Hitoshi Koizumi[1,2,3,*], Chigusa Nakahashi-Oda[1,4,**], Satoshi Fujiyama[1,2], Xuewei Ng[1,5], Hanbin Lee[1,6], Fumie Abe[7], Jinao Li[1,2], Yan Xu[1,2], Takehito Sugasawa[8], Kazuko Tajiri[9], Taketaro Sadahiro[10], Masaki Ieda[10], Keiji Tabuchi[3], Kazuko Shibuya[1,4], Akira Shibuya[1,4,11,**]

[1]Department of Immunology, Institute of Medicine, University of Tsukuba; Tsukuba, Ibaraki, Japan.
[2]Doctoral Program of Biomedical Sciences, Graduate School of Comprehensive Human Sciences, University of Tsukuba; Tsukuba, Ibaraki, Japan.
[3]Department of Otolaryngology–Head and Neck Surgery, Institute of Medicine, University of Tsukuba; Ibaraki, Japan.
[4]R&D Center for Innovative Drug Discovery, University of Tsukuba; Tsukuba, Ibaraki, Japan.
[5]Master's Program in Medical Sciences, Graduate School of Comprehensive Human Sciences, University of Tsukuba; Tsukuba, Ibaraki, Japan.
[6]PhD Program in Human Biology, School of Integrative and Global Majors, University of Tsukuba; Tsukuba, Ibaraki, Japan.
[7]TNAX Biopharma Corporation; Tsukuba, Ibaraki, Japan.
[8]Department of Sports Medicine Analysis, Institute of Medicine, University of Tsukuba, Ibaraki, Japan.
[9]Department of Cardiology, National Cancer Center Hospital East, Kashiwa, Chiba, Japan.
[10]Department of Cardiology, Keio University School of Medicine, Shinjuku, Tokyo, Japan.
[11]Life Science Center for Survival Dynamics, Tsukuba Advanced Research Alliance (TARA), University of Tsukuba; Ibaraki, Japan.

*These two authors contributed equally to this work.

**Corresponding authors

Chigusa Nakahashi-Oda: 1-1-1 Tennodai, Tsukuba-city, Ibaraki, Japan 305-8575; +81-29-853-3281; chigusano@md.tsukuba.ac.jp

Akira Shibuya: 1-1-1 Tennodai, Tsukuba-city, Ibaraki, Japan 305-8575; +81-29-853-3281; ashibuya@md.tsukuba.ac.jp

Conflict of interest: FA is an employee of TNAX Biopharma Corporation. KS and AS own a stake in TNAX Biopharma Corporation. NN is an employee of Daiichi Sankyo at present.

Abstract

Acute ischemic organ diseases such as acute myocardial infarction and acute kidney injury often result in irreversible tissue damage and progress to chronic heart failure (CHF) and chronic kidney disease (CKD), respectively. However, the molecular mechanisms underlying the development of CHF and CKD remain incompletely understood. Here, we show that mice deficient in CD300a, an inhibitory immunoreceptor expressed on myeloid cells, showed enhanced efferocytosis by tissue-resident macrophages and decreased damage-associated molecular patterns and pathogenic SiglecF^{hi} neutrophils, resulting in milder inflammation-associated tissue injury than wild-type mice after ischemia and reperfusion (IR). Notably, we uncovered that CD300a-deficiency on SiglecF^{lo} neutrophils increased the signal transducer and activator of transcription 3-mediated production of pro-angiogenic and anti-fibrotic factors, resulting in milder adverse remodeling after IR. Our results demonstrated that CD300a plays an important role in the pathogenesis of ischemic tissue injury and adverse remodeling in the heart and kidney.

Introduction

Acute myocardial infarction (AMI) is caused by the occlusion of a coronary artery by plaque or thrombus. Percutaneous coronary intervention and coronary artery bypass grafting are widely used to treat AMI and have improved survival rates; however, the number of patients progressing to chronic heart failure (CHF) is rapidly increasing worldwide (1). Acute kidney injury （AKI） is also caused by ischemia and reperfusion (IR) due to therapy or sporadic arterial occlusion; this results in either reversible or irreversible tissue damage (2). AKI is a complication of various diseases, such as heart failure (called cardiorenal syndrome (3)(4), liver failure, and sepsis in patients admitted to hospital, where the prevalence of AKI in patients in the intensive care unit sometimes exceeds 50% (5). AKI often progresses to chronic kidney disease (CKD), which is defined as renal dysfunction that has persisted for more than 3 months (5) .

Within the first few hours of cardiac or renal IR, a large number of cardiomyocytes and tubular epithelial cells die and release damage-associated molecular patterns (DAMPs) such as high-mobility group box 1 (HMGB-1), interleukin (IL)-1α, nucleic acids, and adenosine triphosphate (ATP) (6), which induce inflammation by activating tissue-resident myeloid cells and recruiting inflammatory myeloid cells such as neutrophils and inflammatory monocytes (7). Although the inflammatory responses that accompany angiogenesis and fibrosis are necessary for proper tissue repair, persistent excessive inflammation caused by the subsequent reperfusion exacerbates tissue damage and fibrosis, leading to tissue scarring in the infarcted area, followed by the development of CHF or CKD (5)(8). However, the molecular mechanisms underlying the development of CHF and CKD remain incompletely understood. Moreover, no effective therapy has yet been established to treat cardiac and renal IR-induced injury (IRI) and prevent progression to CHF and CKD, respectively.

Recent studies have reported a unique neutrophil subset highly expressing the cell-surface protein sialic acid-binding immunoglobulin-type lectin F (SiglecF, homolog of human Siglec-8) in the mouse heart after AMI (9)(10). Furthermore, a single-cell transcriptome analysis of murine heart tissue 3 days after AMI has demonstrated the existence of two distinct subsets of neutrophils expressing high or low amounts of SiglecF (i.e., SiglecF^{hi} and SiglecF^{lo}) (10). SiglecF^{hi} neutrophils have also been identified in injured murine lung and kidney tissue; they produce pro-inflammatory and pro-fibrotic cytokines and participate in aberrant tissue remodeling (11)(12). In contrast, however, the functional role of SiglecF^{lo} neutrophils in the pathology of ischemic organ diseases remains unclear, although it has been postulated that their function is similar to that of circulating neutrophils (10).

CD300-family molecules are encoded by eight genes in humans and 12 genes in mice (13) and preferentially expressed on myeloid cells, either activating or inhibiting innate immune responses. One of the family members— CD300a in mice and CD300A in humans— contains the immunoreceptor tyrosine-based inhibitory motif (ITIM) in the cytoplasmic region (14) and mediates an inhibitory signal (15). Phosphatidylserine (PS) exposed on the plasma membrane of dead cells is a functional ligand for CD300a (16). Mice deficient in CD300a on mast cells show prolonged survival in the cecal ligation and puncture sepsis model via augmented secretion of mast-cell-derived chemoattractant and neutrophil recruitment (17). In addition, mice deficient in CD300a on $CX_3CR_1^+CD103^-CD11b^+$ dendritic cells upregulates IFN-β-dependent regulatory T (Treg)-cell expansion in the barrier tissues such as the intestine, skin, and airway (18). On the other hand, CD300a on macrophages suppresses CD300b-mediated efferocytosis by inhibiting activation of the CD300b-associated adaptor DNAX activation protein 12 (DAP12) (19). CD300a deficiency enhances efferocytosis by inflammatory monocytes infiltrating into the brain after middle cerebral artery occlusion (MCAO) and reperfusion in mice; this results in amelioration of the neurological deficit (19).

These results raise the question whether CD300a blockade can ameliorate ischemic damage in organs other than the brain via enhanced efferocytosis.

Here, we showed that CD300a-deficiency reduced inflammation-associated tissue damage and dysfunctions in the heart and kidney after IR via increasing the efferocytosis by tissue-resident macrophages and decreasing the release of DAMPs from dead cells. Moreover, we unveiled the important role of SiglecF^{lo} neutrophils in remodeling after IRI. CD300a-deficiency on SiglecF^{lo} neutrophils increased signal transducer and activator of transcription 3 (STAT3) phosphorylation and increased the production of pro-angiogenic and anti-fibrotic factors after IR.

Results

CD300a-deficiency reduces cardiac IRI and adverse remodeling.

To examine whether CD300a is involved in the pathogenesis of cardiac IRI, we established a murine model of myocardial infarction and reperfusion (MI/R) by the occlusion of the left anterior descending artery (LAD) for 1 h followed by arterial reperfusion (Figure 1A). The plasma level of cardiac troponin I (cTnI), which is released by injured cardiomyocytes, was significantly lower in *Cd300a*$^{-/-}$ mice than in wild-type (WT) mice at 3 h after MI/R (Figure 1B). Histological analysis using Evans blue and triphenyl tetrazolium chloride staining revealed that the proportion of the infarct area within the ischemic area was significantly smaller in the hearts of *Cd300a*$^{-/-}$ mice than in those of WT mice at 24 h after MI/R (Figures 1C and S1A). Immunohistochemical analysis showed that the numbers of capillary vessels and CD31^{+} endothelial cells were significantly greater at the ischemic area in *Cd300a*$^{-/-}$ mice than in WT mice at 3 and 14 days after MI/R (Figures 1D and S1B). Moreover, the analysis demonstrated a significant increase in the proportion and the number of fibroblast-specific protein 1 (FSP1)–expressing fibroblasts, which have a pro-angiogenic function in wound healing in murine and human hearts after MI (20), and a significant decrease in the proportion and the number of α-smooth muscle actin (αSMA)–expressing pro-fibrotic fibroblasts, in the ischemic area s of cardiac tissue of *Cd300a*$^{-/-}$ mice than in that of WT mice at 3 days after MI/R (Figures 1E and S1C), consistent with the observation of decreased fibrotic area in *Cd300a*$^{-/-}$ mice than in WT mice at 8 weeks after MI/R (Figure 1F). Echocardiography showed that the left ventricular end-systolic dimension was significantly smaller, and the left ventricular fractional shortening (LVFS) and left ventricular ejection fraction (LVEF) were significantly larger in *Cd300a*$^{-/-}$ mice than in WT mice at 4 to 8 weeks after MI/R (Figure 1G). To determine which cell type expressing CD300a is involved in the cardiac function after MI/R, we used *Cd300a*$^{fl/fl}$*Lyz2*-Cre mice and *Cd300a*$^{fl/fl}$*Itgax*-Cre mice,

in which CD300a expression is lacking on phagocytes, including neutrophils and both monocyte-derived and tissue-resident macrophages, and dendritic cells, respectively, in the heart. We found that LVFS and LVEF were increased in *Cd300a*$^{fl/fl}$*Lyz2*-Cre mice, but not in *Cd300a*$^{fl/fl}$*Itgax*-Cre mice, compared to control mice after MI/R (Figure S1D). These results indicate that CD300a deficiency in phagocytes decreases myocardial damage and subsequent fibrosis and improves cardiac function after MI/R.

CD300a-deficiency reduces IR-induced AKI and fibrosis

We next analyzed AKI, in which the renal arteries were clamped bilaterally for 15 min followed by reperfusion (biIRI) in *Cd300a*$^{fl/fl}$ and *Cd300a*$^{fl/fl}$*Lyz2*-Cre mice (Figure 2A), in which CD300a expression is lacking on the phagocytes in the kidney (Figure S2A); this is a similar expression profile to that of *Cd300a*$^{-/-}$ mice in the heart. Levels of neutrophil gelatinase-associated lipocalin (NGAL), which is released from damaged tubular epithelial cells (21), were significantly lower in *Cd300a*$^{fl/fl}$*Lyz2*-Cre mice than in *Cd300a*$^{fl/fl}$ mice 6 h and 3 days after biIRI (Figure 2B). Blood urea nitrogen (BUN) and plasma creatinine concentrations were also significantly lower in *Cd300a*$^{fl/fl}$*Lyz2*-Cre mice than in *Cd300a*$^{fl/fl}$ mice one and 2 days after biIRI (Figure 2C). Histological analysis of the corticomedullary junction demonstrated that acute tubular necrosis (ATN) scores, as determined by the sum of scores for tubular necrosis, intratubular debris deposition, and loss of the brush border of tubular epithelial cells, were significantly lower in *Cd300a*$^{fl/fl}$*Lyz2*-Cre mice than in *Cd300a*$^{fl/fl}$ mice 2 days after biIRI (Figure 2D). Moreover, although the proportion of kidney-injury-molecule-1-positive (KIM-1$^+$; i.e. damaged proximal tubular epithelial cells) was comparable between the two genotypes of mice 2 and 7 days after biIRI (Figure S2B), the expression of phosphorylated histone H3 (p-H3), a marker of cell-cycle arrest at G_2/M transition, in KIM-1$^+$ tubular epithelial cells was significantly lower in *Cd300a*$^{fl/fl}$*Lyz2*-Cre

mice than in *Cd300a*$^{fl/fl}$ mice 2 and 7 days after biIRI (Figure 2E). These p-H3-expressing tubular epithelial cells with maladaptive repair secrete profibrotic factors (22) . Indeed, we found that transforming growth factor-β (*Tgfb*), *Il1b*, and connective tissue growth factor (*Ctgf*) expression was significantly lower in the kidneys of *Cd300a*$^{fl/fl}$*Lyz2*-Cre mice than of *Cd300a*$^{fl/fl}$ mice 5–7 days after biIRI (Figure 2F). Furthermore, 28 days after biIRI, renal fibrosis, as analyzed by Masson's trichrome and Sirius red staining, was significantly milder in *Cd300a*$^{fl/fl}$*Lyz2*-Cre mice than in *Cd300a*$^{fl/fl}$ mice (Figures 2G and S2C).

Further analysis of the CD300a involvement in the development of renal fibrosis, we used a two-step unilateral IRI (uIRI) model (23), in which the left renal artery was clamped for 20 min (longer than for biIRI) and then reperfused, followed by removal of the right kidney on day 14 after uIRI (Figure S2D) in *Cd300a*$^{fl/fl}$ and *Cd300a*$^{fl/fl}$*Lyz2*-Cre mice. Plasma NGAL concentrations 24 h after uIRI were significantly lower in *Cd300a*$^{fl/fl}$*Lyz2*-Cre mice than in *Cd300a*$^{fl/fl}$ mice (Figure S2E). Just after the removal of the right kidney on day 14 in uIRI, BUN and creatinine concentrations were significantly lower in *Cd300a*$^{fl/fl}$*Lyz2*-Cre mice than in *Cd300a*$^{fl/fl}$ mice (Figure S2F). Importantly, the degree of fibrosis on day 49 in uIRI was significantly milder in *Cd300a*$^{fl/fl}$*Lyz2*-Cre mice than in *Cd300a*$^{fl/fl}$ mice (Figure S2G). Together, these results suggest that the CD300a deficiency on phagocytes decreases the production of pro-inflammatory and pro-fibrotic cytokines in the kidney, thus ameliorating AKI and subsequent fibrosis similar to cardiac injury due to MI/R.

CD300a-deficiency enhances efferocytosis and ameliorates inflammation-associated tissue damage after cardiac and renal IRI.

To examine how CD300a regulates myocardial damage and subsequent fibrosis after MI/R, we determined the expression of CD300a on myeloid cells in cardiac tissue after MI/R. CD300a expression was confirmed on neutrophils ($CD11b^+Ly6G^+$), monocyte-derived

189 macrophages ($CD11b^+Ly6G^-Ly6C^+$), and tissue-resident macrophages ($CD11b^+Ly6G^-Ly6C^-$
190 $CD64^+$) in the cardiac tissue of naïve WT mice, and these expressions— particularly on the
191 tissue-resident macrophages—were upregulated at 3 days after MI/R (Figure S3A). To
192 examine whether CD300a was involved in the efferocytosis after MI/R, we intravenously
193 administered PSVue-643, a near-infrared fluorescent probe for the detection of PS-expressing
194 dead cells, to WT and *Cd300a*$^{-/-}$ mice immediately after MI/R and used flow cytometry to
195 evaluate efferocytosis by myeloid cells (Figure 3A). *Cd300a*$^{-/-}$ mice showed a significantly
196 higher proportion of tissue-resident macrophages expressing PSVue-643 fluorescence than
197 did WT mice at 3 h after MI/R; in both types of mice, neither neutrophils nor inflammatory
198 monocytes showed PSVue-643 fluorescence (Figure 3B), indicating that *Cd300a*$^{-/-}$ tissue-
199 resident macrophages showed enhanced efferocytosis after MI/R. In line with these results,
200 *Cd300a*$^{-/-}$ mice showed lower plasma levels of DAMPs such as HMGB-1 and IL-1α in the
201 coronal sinus and had significantly fewer tissue-infiltrating inflammatory cells, including
202 neutrophils and monocyte-derived macrophages, than WT mice at 6 h and 3 days,
203 respectively, after MI/R (Figures 3C and S3B).
204 To investigate the role of CD300a in efferocytosis after IRI in the kidney, we
205 transferred BM cells from td*Tomato*$^{fl/fl}$*Lyz2*-Cre or *Cd300a*$^{fl/fl}$td*Tomato*$^{fl/fl}$*Lyz2*-Cre mice into
206 irradiated enhanced green fluorescent protein (EGFP)-expressing R26GRR mice. Four weeks
207 later, these mice, in which the transferred phagocytes expressed tdTomato fluorescence, were
208 subjected to biIRI (Figure 3D). Flow cytometric analyses demonstrated that although each
209 myeloid cell population was comparable between the two genotypes of mice 3 h after biIRI
210 (Figure S3C), the population of EGFP-expressing resident macrophages derived from
211 *Cd300a*$^{fl/fl}$td*Tomato*$^{fl/fl}$*Lyz2*-Cre mice was significantly larger than that derived from
212 td*Tomato*$^{fl/fl}$*Lyz2*-Cre mice 3 h after biIRI (Figure 3E). Furthermore, laser scanning confocal
213 microscopy analysis revealed that the EGFP signal was detected in the cytoplasm of the

214 tdTomato^{+} myeloid cells, indicating that these myeloid cells engulfed host-derived dead
215 tissues, and the phagocytic index, as determined by the numbers of EGFP-expressing
216 macrophages and the magnitude of EGFP signals detected in each macrophage, was larger in
217 *Cd300a*$^{fl/fl}$td*Tomato*$^{fl/fl}$*Lyz2*-Cre macrophages than in td*Tomato*$^{fl/fl}$*Lyz2*-Cre macrophages
218 (Figure S3D). These results indicate that mice deficient in CD300a on tissue-resident
219 macrophages showed enhanced efferocytosis in the kidney after biIRI, as was also observed
220 after MI/R. In line with these results, *Cd300a*$^{fl/fl}$*Lyz2*-Cre mice showed lower levels of
221 HMGB-1 in the plasma and the expressions of proinflammatory cytokines *Il6, Tnfa, and Il1b*,
222 and a smaller number of tissue-infiltrating inflammatory cells, including monocyte-derived
223 macrophages and neutrophils, than *Cd300a*$^{fl/fl}$ mice after biIRI (Figures 3F, and S3E and
224 S3F).

225 Milk-fat globulin protein E8 (MFG-E8) mediates efferocytosis via crosslinking PS on
226 dead cells to αvβ3 integrin on macrophages. However, MFG-E8 mutated at residue 89 (D89E-
227 MFG-E8), which binds to PS, but not αvβ3, inhibits PS receptor-mediated efferocytosis (24).
228 D89E-MFG-E8 or a control protein (EPT-MFG-E8; mutant MFG-E8 with altered binding
229 regions for PS) was i.v. injected into WT or *Cd300a*$^{-/-}$ mice immediately after MI/R. Whereas
230 EPT-MFG-E8 administration into mice resulted in significantly lower plasma levels of cTnl
231 and a significantly higher LVEF in *Cd300a*$^{-/-}$ mice than in WT mice, D89E-MFG-E8
232 administration resulted in comparable plasma levels of cTnl and a comparable LVEF in the
233 two genotypes of mice (Figures 3G and 3H). D89E-MFG-E8 administration also increased
234 plasma NGAL, BUN, and creatinine concentrations in *Cd300a*$^{fl/fl}$*Lyz2*-Cre mice to levels
235 comparable to those seen in *Cd300a*$^{fl/fl}$ mice 24 h and 48 h after biIRI (Figures 3I, 3J, S3G, and
236 S3H). Moreover, the *Tgfb* expression in the kidney and the degree of renal fibrosis, as analyzed
237 by histological analysis using Masson's trichrome staining, in *Cd300a*$^{fl/fl}$*Lyz2*-Cre mice was
238 increased to a level seen in *Cd300a*$^{fl/fl}$ mice after D89E-MFG-E8 treatment 28 days after biIRI,

239 respectively (Figures 3K and 3L). Together, these results suggest that increased efferocytosis
240 due to CD300a deficiency on tissue-resident macrophages reduced tissue damage
241 accompanying the reduction of DAMPs release from dead cells and tissue-infiltrating cells,
242 ameliorates cardiac and renal injuries, and the following aberrant remodeling after IR through
243 a similar mechanism.
244
245 **CD300a-deficiency upregulates pro-angiogenic and anti-fibrotic gene expressions in**
246 **SiglecF^{lo} neutrophils.**
247 Since CD300a is expressed on neutrophils as well as macrophages, we analyzed the role
248 of CD300a on neutrophils in the pathogenesis of cardiac function after MI/R by depleting
249 neutrophils. WT and *Cd300a*$^{-/-}$ mice were i.v. injected with a depleting anti-Ly6G mAb on
250 day -1, 0, and 1 after MI/R, and immune cells in the heart were analyzed for cell surface
251 expression of Gr-1 by an anti-Gr-1 mAb and intracellular expression of Ly6G by the anti-
252 Ly6G mAb by flow cytometry. On day 3 after MI/R, both cell surface Gr-1 and intracellular
253 Ly6G were not detected in the neutrophil population in the heart (Figure S4A). In contrast,
254 the monocyte-derived macrophage population（CD11b^{+}Ly6C^{+}Gr-1^{-}Ly6G^{-}）was not altered
255 by injection of the anti-Ly6G mAb (Figure S4A), indicating that neutrophils but not
256 macrophages were depleted in the heart on day 3 after MI/R. We found that the anti-Ly6G
257 mAb treatment decreased capillary density and FSP1–expressing fibroblasts at 3 days after
258 MI/R in *Cd300a*$^{-/-}$ mice to a level comparable to that in WT mice (Figures 4A, 4B, and
259 S4B). Furthermore, compared to WT mice, control mAb injection increased LVFS and LVEF
260 at day 7 and decreased scar area at 4 weeks post MI/R in *Cd300a*$^{-/-}$ mice, but administration
261 of anti-Ly6G mAb abolished these differences between *Cd300a*$^{-/-}$ and WT mice (Figures 4C
262 and 4D), suggesting that CD300a on neutrophils is involved in angiogenesis, the
263 development of fibrosis, and cardiac function after MI/R. To confirm this idea, we transferred

264 *Cd300a*$^{-/-}$ or WT neutrophils into WT mice immediately and 3 days after MI/R. We found
265 that mice that received *Cd300a*$^{-/-}$ neutrophils showed higher capillary density in the cardiac
266 tissue than those that received WT neutrophils (Figure 4E). Together, these results suggest
267 that *Cd300a*$^{-/-}$ neutrophils promote angiogenesis and cardiac function after MI/R.
268 Recent studies revealed that SiglecF^{hi} neutrophils are increased in the cardiac tissue after
269 myocardial infarction in mice (9)(10). Whereas most neutrophils in the BM and peripheral
270 blood of WT and *Cd300a*$^{-/-}$ mice were found to express no, or a low level of, SiglecF
271 (SiglecF^{lo}), those in the post-MI/R cardiac tissue of both genotypes of mice were found to
272 highly express SiglecF (SiglecF^{hi}) (Figure 4F). However, *Cd300a*$^{-/-}$ mice exhibited a
273 significantly lower proportion of SiglecF^{hi} neutrophils and a significantly higher proportion
274 of SiglecF^{lo} neutrophils in injured cardiac tissue than in WT mice (Figure 4F). Furthermore,
275 when LVEF at day 3 post-MI/R was used as a measure, a larger proportion of SiglecF^{lo}
276 neutrophils was positively correlated with better cardiac function (Figure 4G), suggesting that
277 SiglecF^{lo} neutrophils play an important role in angiogenesis and cardiac function after MI/R.
278 To further characterize *Cd300a*$^{-/-}$ neutrophils involved in the pathology of MI/R injury,
279 we used RNA-sequence analysis to compare the gene expression profiles of the two
280 neutrophil subsets purified from cardiac tissue from the two genotypes of mice at day 3 post-
281 MI/R. Whereas the SiglecF^{hi} neutrophils from both genotypes of mice showed a similar gene
282 expression profile, those of the SiglecF^{lo} neutrophils differed (Figures 4H, S4C, and S4D).
283 The most prominent genes upregulated in *Cd300a*$^{-/-}$ SiglecF^{lo} neutrophils were associated
284 with angiogenesis (Figures 4I, 4J, and S4E). For example, the mRNA expression of *Prok2*
285 and *Chil1*, which both encode pro-angiogenic factors, was upregulated more in *Cd300a*$^{-/-}$
286 SiglecF^{lo} neutrophils than in WT SiglecF^{lo} neutrophils (Figure 4K). However, WT and
287 *Cd300a*$^{-/-}$ SiglecF^{lo} neutrophils from the peripheral blood showed comparable expression

levels of these mRNAs (Figure S4F). In addition, genes associated with collagen degradation in the extracellular matrix, including genes encoding members of the matrix metalloproteinase family and the ADAM metallopeptidase family, were upregulated in *Cd300a*$^{-/-}$ SiglecF^{lo} neutrophils (Figures 4L and 4M). These results suggest that CD300a regulates the expression of genes encoding pro-angiogenic and anti-fibrotic factors in SiglecF^{lo} neutrophils.

In contrast, SiglecF^{hi} neutrophils showed upregulation of genes associated with inflammatory responses and fibrosis (Figures S4G–J). For example, the mRNA expression levels of genes encoding pro-inflammatory cytokines, such as tumor necrosis factor-α (*Tnf*), interleukin-1β (*Il1b*), interleukin-6 (*Il6*), and the pro-fibrotic factor *Tgfb1*, were significantly higher in SiglecF^{hi} neutrophils than in SiglecF^{lo} neutrophils, although the expression levels of those genes were comparable between WT and *Cd300a*$^{-/-}$ neutrophils (Figures S4K and S4L). These results indicate that SiglecF^{hi} neutrophils play pathogenic roles by exacerbating inflammation and fibrosis, regardless of CD300a expression, after MI/R.

Of note, we also found that the SiglecF^{hi} neutrophil population was smaller, and the SiglecF^{lo} neutrophil population was larger in *Cd300a*$^{fl/fl}$*Lyz2*-Cre mice than in *Cd300a*$^{fl/fl}$ mice also in the kidney 14 days after biIRI (Figure S4M), suggesting a similar functional role of CD300a on neutrophils in the kidney after biIRI, as observed in the heart after MI/R.

CD300a inhibits STAT3 phosphorylation in SiglecF^{lo} neutrophils.

To examine how *Cd300a*$^{-/-}$ mice had a lower proportion of SiglecF^{hi} neutrophils than did WT mice, we stimulated WT or *Cd300a*$^{-/-}$ BM neutrophils with the supernatant from a suspension of WT mouse cardiac tissue collected before, or 6 h after, MI/R (Figure S5A). The supernatant of cardiac tissue after MI/R, but not that from naïve heart, induced the generation of SiglecF^{hi} neutrophils, even though the WT and *Cd300a*$^{-/-}$ BM neutrophil

populations contained comparable proportions of SiglecF^{hi} neutrophils (Figure S5B). This suggests that the transition of SiglecF^{lo} to SiglecF^{hi} neutrophils was induced by extrinsic factors in the heart after MI/R. We hypothesized that DAMPs, such as HMGB-1 or IL-1α after MI/R (Figure 3C) may induce the generation of SiglecF^{hi} neutrophils in the injured heart. However, neither HMGB-1 nor IL-1α had any effect on the generation of SiglecF^{hi} neutrophils when neutrophils purified from the BM were stimulated with DAMPs alone (Figure S5C). By contrast, SiglecF^{hi} neutrophils were generated when BM neutrophils were stimulated with the culture supernatant of the naïve cardiac tissues after stimulation with IL-1α, but not HMGB-1 (Figures 5A and 5B), suggesting that IL-1α indirectly induces the generation of SiglecF^{hi} neutrophils by stimulating cardiac cells rather than neutrophils.

IL-1α induces the production of granulocyte-macrophage colony-stimulating factor (GM-CSF) and granulocyte colony-stimulating factor (G-CSF) by fibroblasts in arthritis, arthrofibrosis and skin fibrosis (25)(26). Similarly, we found here that stimulation of WT cardiac cells with IL-1α induced the production of GM-CSF and G-CSF (Figure 5C). Stimulation of purified BM neutrophils with GM-CSF or G-CSF induced the generation of SiglecF^{hi} neutrophils, with the WT and *Cd300a*$^{-/-}$ BM neutrophil populations containing comparable proportions of SiglecF^{hi} neutrophils (Figure 5D). Since IL-1α expression was lower in *Cd300a*$^{-/-}$ mice than in WT mice (Figure 3C) because of enhanced efferocytosis in the former after MI/R (Figure 3B), these results suggest that the lower release of IL-1α in *Cd300a*$^{-/-}$ mice resulted in reduced production of G-CSF and GM-CSF, which in turn resulted in the generation of fewer SiglecF^{hi} neutrophils.

To elucidate how CD300a regulates gene expression in SiglecF^{lo} neutrophils, the signals regulated by CD300a in SiglecF^{lo} neutrophils were predicted by Ingenuity Pathway Analysis using gene sets enriched in *Cd300a*$^{-/-}$ SiglecF^{lo} neutrophils compared with those in WT SiglecF^{lo} neutrophils, as determined by using RNA-seq data. Because CD300a is localized on

the cell surface and suppresses proximal activating signals derived from nearby localized receptors, we focused on signals from cell-surface receptors. The top two upstream candidates were the genes encoding IL-6 and G-CSF receptor-mediating signaling pathway (Figure 5E), respectively, which activate STAT3 in neutrophils and promote angiogenesis (27)(28). Indeed, the genes upregulated in *Cd300a*$^{-/-}$ SiglecF^{lo} neutrophils were enriched in the STAT3 signaling pathway (Figure S5D). *Cd300a*$^{-/-}$ SiglecF^{lo} neutrophils exhibited a significantly higher proportion of phosphorylated STAT3 than did WT SiglecF^{lo} neutrophils and WT SiglecF^{hi} neutrophils in the cardiac tissue on day 3 post-MI/R (Figure 5F). Stimulation of BM neutrophils with a supernatant from cardiac tissue after MI/R resulted in significantly greater STAT3 phosphorylation (Figure 5G) and upregulation of the pro-angiogenic genes *Prok2* and *Chil1* in *Cd300a*$^{-/-}$ neutrophils compared with WT neutrophils (Figure 5H), suggesting that CD300a suppresses the expression of pro-angiogenic and anti-fibrotic genes by inhibiting STAT3 activation in SiglecF^{lo} neutrophils in cardiac tissue after MI/R. Among the candidate CD300a-targeting signals predicted by the ingenuity pathway analysis, G-CSF stimulation, but not IL-6, increased the phosphorylation of STAT3 and the expressions of *Prok2* and *Chil1* in *Cd300a*$^{-/-}$ BM neutrophils, whereas a STAT3 inhibitor (STAT3i) reduced their expression to levels comparable to those in WT neutrophils (Figure 5I, S5E and S5F), indicating that CD300a inhibits the G–CSF–STAT3 axis for the expressions of *Prok2* and *Chil1* in *Cd300a*$^{-/-}$ BM neutrophils *in vitro.* Moreover, STAT3i abolished the improved LVEF in *Cd300a*$^{-/-}$ mice at day 3 post-MI/R (Figure 5J). Taken together, although other cell types in addition to *Cd300a*$^{-/-}$ BM neutrophils was also involved in the effect of STAT3i *in vivo,* these results suggest that pro-angiogenic genes are induced via the G–CSF–STAT3 axis, which is inhibited by CD300a in SiglecF^{lo} neutrophils and attenuate cardiac dysfunction after MI/R.

CD300a blockade with a neutralizing antibody ameliorates cardiac and renal IRI and adverse remodeling.

To determine whether CD300a blockade ameliorates cardiac and renal IRI, we i.v. injected an anti-CD300a neutralizing mAb or control mAb into WT mice immediately after MI/R and 2 h before biIRI and two-step uIRI. Administration of this antibody did not affect the percentage of neutrophil and macrophage populations in the kidney 1 and 7 days after biIRI (Figure S6A) (29). Consistent with our earlier observations in *Cd300a*$^{-/-}$ mice (Figure 1), treatment with the anti-CD300a mAb reduced the plasma cTnI level, increased angiogenesis, improved LVFS and LVEF, and reduced fibrosis compared with control antibody injection after MI/R (Figures 6A-D). To determine whether these effects of anti-CD300a mAb were caused by enhanced efferocytosis, we used αMHC-GFP mice, in which only mature cardiomyocytes express GFP (30). Treatment with the anti-CD300a mAb enhanced efferocytosis by resident macrophages, but not neutrophils and monocyte-derived macrophages, as determined by GFP expression by flow cytometry, compared to that of the control antibody (Figure 6E).

To analyze the effect of the anti-CD300a mAb on IRI in the kidney, we used the BM chimeric mice reconstituted with WT or *Cd300b*$^{-/-}$ BM cells (Figure 3D). These chimeric mice were i.v. received the anti-CD300a mAb or control mAb at 2 h before biIRI. Similarly to the resident macrophages from *Cd300a*$^{fl/fl}$td*Tomato*$^{fl/fl}$*Lyz2*-Cre mice (Figure 3E), efferocytosis by resident macrophages was enhanced (Figure 6F), and plasma BUN and creatinine concentrations and ATN scores on histology at 24 h and 48 h, respectively, after biIRI were significantly lower in mice treated with the anti-CD300a mAb than in those treated with the control mAb (Figures 6G, H). Moreover, renal fibrosis at 28 days after biIRI was significantly milder in mice treated with the anti-CD300a mAb than in those treated with

the control antibody (Figure 6I). By using a two-step uIRI, during the 49-day observation period, plasma BUN and creatinine concentrations were significantly lower, and the degree of renal fibrosis was significantly milder, in mice treated with the anti-CD300a mAb than in mice treated with the control antibody (Figures S6B and S6C). Moreover, treatment with the anti-CD300a mAb, even 3 h after uIRI, ~~significantly~~ improved renal function (Figure S6D).

CD300a on macrophages suppresses CD300b-mediated efferocytosis by inhibiting the CD300b-associated DAP12 activation *in vitro* and neurological damage after MCAO in mice (19). We examined whether this is also the case in IRI in the kidney. As expected, the anti-CD300a mAb had no effect on efferocytosis, plasma BUN and creatinine concentration levels, and renal fibrosis in CD300b-deficient mice (Figures 6F, 6G, and 6I). These results suggest that CD300a blockade by the neutralizing anti-CD300a mAb enhanced CD300b-mediated efferocytosis and ameliorated both tissue injury and fibrosis after cardiac and renal IR.

A humanized anti-CD300A mAb ameliorates renal IRI in humanized mice.

By using a public data set (Nephroseq v5, http://v5.nephroseq.org) of gene expression profiles in CKD patients, *CD300A* expression was significantly higher in patients with CKD due to diabetic nephropathy (DN) and focal segmental glomerulosclerosis (FSGS) than in control patients (Figure 7A). In addition, Spearman's correlation analysis demonstrated that the expression level of *CD300A* was negatively correlated with glomerular filtration rate (GFR) but positively correlated with the plasma concentration of creatinine (Figure 7B). These results suggest the possibility that CD300A is involved in the transition to CKD after AKI in humans.

We generated a neutralizing mouse anti-human CD300A mAb, named TX113, that binds to transfectants stably expressing CD300A (31). We further generated a humanized

412 neutralizing mAb based on the complementarity-determining regions of TX113 with the
413 human IgG1-Fc portion with a mutated amino acid at residues 234 and 235 from Leucine to
414 Alanine (named TNAX103) (32). We cocultured peripheral blood monocytes with dead
415 Jurkat cells, which had been labeled with a pH-sensitive fluorescent dye (pHrodo), in the
416 presence of TNAX103 or control mAb, and we analyzed efferocytosis by confocal laser
417 scanning microscopy. In these experiments, the phagocytic index of monocytes was
418 significantly higher in the presence of TNAX103 than in the presence of the control mAb
419 (Figure 7C). To clarify the role of TNAX103 in the development of AKI after IRI, NOD
420 SCID mice deficient in the common γ chain of the interleukin (IL)-2 receptor (NOG mice)
421 with transgenic expression of human granulocyte-macrophage colony-stimulating factor
422 (GM-CSF) and IL-3 (named NOG-EXL mice) were transplanted with human $CD34^+$ stem
423 cells (Figure 7D). Ten weeks later, we confirmed the engraftment of human $CD45^+$
424 hematopoietic cells expressing CD300A in the peripheral blood of naïve mice (Figure S7)
425 and $CD14^+$ myeloid cells expressing CD300A in the kidney 48 h after biIRI (Figure 7E).
426 These mice were administered TNAX103 or a control mAb 2 h before biIRI. Forty-eight h
427 after biIRI, plasma NGAL and creatinine concentrations were significantly lower in
428 TNAX103- than in control-mAb-treated mice (Figures 7F and 7G). These results suggest that
429 TNAX103 is potentially useful for the treatment of ischemic organ diseases such as AMI and
430 AKI and the prevention of CHF and CKD.
431

Discussion

Here, we showed that CD300a deficiency ameliorates tissue injury, dysfunction, and fibrosis in the heart and kidney after IR by enhancing efferocytosis by tissue-resident macrophages and decreasing the release of dead cell-derived DAMPs such as IL-1α and or HMGB-1. We previously reported that CD300a blockade ameliorated acute ischemic stroke by IR in mice (19). IRI in the heart and kidney differs from that in the brain in that CD300a blockade enhanced efferocytosis by tissue-resident macrophages in the heart and kidney, but not by inflammatory monocyte-derived macrophages in the brain. The most important finding in the heart and kidney, which was not observed in the brain, is that CD300a blockade also suppressed fibrosis after IR. Recent studies have reported that SiglecF^{hi} neutrophils are elicited at the injured tissue by DAMPs and have a pathogenic function to induce fibrosis by producing profibrotic or proinflammatory cytokines such as TGF-β, TNF-α, and IL-1β, and also by directly producing collagen I in a mouse model of CKD (12). SiglecF^{hi} neutrophils originate from the BM, and after migration from the peripheral blood to injured tissues, they acquire their characteristic gene expression profile associated with pathogenesis of inflammation (10)(33). Recent studies have demonstrated that DAMPs or inflammation-associated cytokines such as GM-CSF and TGF-β induce the generation of pathogenic SiglecF^{hi} neutrophils in asthma and CKD (11)(12). Here, we found that one of the DAMPs, IL-1α, stimulated G-CSF and GM-CSF production in the cardiac tissue, likely by fibroblasts (25)(26), and that these cytokines induced the generation of SiglecF^{hi} neutrophils after MI/R. Since we showed here that IL-1α induced the generation of SiglecF^{hi} neutrophils at comparable levels in WT and *Cd300a*$^{-/-}$ mice, the decrease of SiglecF^{hi} neutrophils in *Cd300a*$^{-/-}$ mice after MI/R may have been caused by a decreased amount of IL-1α in the infarct lesion in the heart. We also showed that the SiglecF^{hi} neutrophil population was lower in *Cd300a*$^{fl/fl}$*Lyz2*-Cre mice than in *Cd300a*$^{fl/fl}$ mice in the kidney after biIRI, suggesting a similar mechanism of tissue injury and

457 fibrosis in the kidney as in the heart. Regardless, CD300a deficiency decreased the pathogenic
458 SiglecF^{hi} neutrophil population, contributing in part to the reduction of tissue injury, fibrosis,
459 and organ dysfunction after MI/R and likely after renal IR.

460 DAMPs such as HMGB1 are also known to induce endoplasmic reticulum stress and
461 G_2/M arrest of tubular epithelial cells (6)(22). These cells with G_2/M arrest express *Tgfb* and
462 *Ctgf* through an interaction between cyclin G1 and cyclin-dependent kinase 5, as well as via
463 the histone deacetylase 9 (HDAC9)/signal transducer and activator of the transcription 1
464 (STAT1) signaling pathway, causing CKD with fibrosis (34)(35). Here, we showed that
465 HMGB1 was decreased at 24 h after IR, and that this was followed by a decrease in the number
466 of p-H3^{+} tubular cells with G_2/M arrest 2 days after IR and a decrease in *Tgfb*, *Ctgf,* and *Il1b*
467 expression in the kidney 5–7 days after IR. These results suggest that the decrease in DAMPs
468 due to enhanced efferocytosis may have resulted in the reduction of maladaptive tubular repair
469 in addition to the decrease in SiglecF^{hi} neutrophils, thereby suppressing the production of
470 fibrosis-inducing cytokines and preventing fibrosis.

471 In contrast to the functional characteristics of SiglecF^{hi} neutrophils, those of SiglecF^{lo}
472 neutrophils remain to be fully determined. Here, we uncovered that SiglecF^{lo} neutrophils
473 express genes encoding angiogenic and anti-fibrotic cytokines such as Prok2, Chil1, and
474 MMP9. Notably, we showed that CD300a regulates the production of these cytokines by
475 SiglecF^{lo} neutrophils by inhibiting STAT3 phosphorylation. Thus, CD300a-deficiency
476 promotes the production of these cytokines, thereby contributing in part to the reduction of
477 adverse remodeling with fibrosis and cardiac dysfunction after MI/R. Together, these results
478 suggest that CD300a-deficiency prevents the development of CHF after MI/R via both
479 SiglecF^{hi} and SiglecF^{lo} neutrophils: CD300a deficiency in tissue-resident macrophages
480 increased efferocytosis and thereby decreased DAMPs, which directly reduced inflammation-
481 associated tissue injury and indirectly reduced it via decreasing the generation of pathogenic

SiglecF^{hi} neutrophils. In addition, decreasing DAMPs via enhanced efferocytosis increased the proportion of SiglecF^{lo} neutrophils with proangiogenic and anti-fibrotic characteristics, resulting in preventing fibrosis and following CHF. Since the SiglecF^{hi} and SiglecF^{lo} neutrophils were lower and higher, respectively, in *Cd300a*$^{fl/fl}$*Lyz2*-Cre mice than in *Cd300a*$^{fl/fl}$ mice in the kidney after biIR, CD300a on neutrophils, as well as tissue-resident macrophages, likely plays an important role in the development of AKI and following renal fibrosis.

We showed that a humanized anti-CD300A mAb enhanced efferocytosis by human monocytes in vitro. To study the role of efferocytosis in the development of IRI in humans, we used humanized mice. Treatment of the humanized mice with the humanized anti-CD300A mAb improved AKI after IR. Because the humanized anti-CD300A mAb specifically binds to human CD300A but not mouse CD300a, these results suggest that the mAb enhanced efferocytosis of mouse dead cells by tissue-resident human macrophages and suppressed the inflammation induced by DAMPs, preventing tissue damage such as that to tubular epithelial cells and glomeruli in the mouse kidney. This AKI model using humanized mice is useful for studying the role of humanized CD300A mAb in efferocytosis via human macrophages *in vivo*. Our results suggest that the anti-CD300A mAb can be used to treat ischemic organ diseases, including AMI, AKI, and others, and for the prevention of the transition to CHF and CKD.

Methods

Sex as a biological variable.

Our study exclusively examined male mice. It is unknown whether the findings are relevant for female mice.

Mice.

C57BL/6J were purchased from Clea Japan (Tokyo, Japan). *Cd300a*$^{-/-}$ (17), *Cd300a*$^{fl/fl}$, *Lyz2*-Cre, *Cd300a*$^{fl/fl}$*Lyz2*-Cre (19), *Cd300b*$^{-/-}$ (19), R26GRR (*Rosa26*$^{CAG\text{-}EGFP/tdsRed}$) (36), td*Tomato*$^{fl/fl}$ (*Gt* (*ROSA*)*26Sor*$^{tm14(CAG\text{-}tdTomato)Hze}$) (37) and αMHC-GFP mice (30) mice on the C57BL/6 background were described previously. NOG mice expressing transgenic human GM-CSF and IL-3 (NOG-EXL), which had been transferred with human cord blood CD34^{+} cells, were purchased from In-Vivo Science (Tokyo, Japan). The chimerism rate of human cells in peripheral blood was greater than 26 %.

Ischemia and reperfusion models in the heart and kidney.

Male mice (8-12 weeks old, 23-29g) were used to induce MI/R (38), biIRI, and two-stage uIRI. Mice were anesthetized by intraperitoneal administration of 0.2 mg/kg of medetomidine, 0.8 mg/kg of midazolam, and 0.5 mg/kg of butorphanol. For the induction of MI/R, mice were intubated and ventilated at 140 respirations/min and 18 cm H_2O of peak pressure max by ventilator (Mouse Ventilator Minivent Type 845, Harvard Apparatus). Anesthesia was maintained with 2.0-2.5% isoflurane with a heating pad during the surgery. A 4th intercostal thoracotomy was performed to expose the heart. A silicon tube (PE-10 tube) and left anterior descending artery (LAD) were ligated with a 7-0 silk and after 60 min, the silicon tube and the suture are removed to allow reperfusion. For neutrophil depletion, anti-Ly6G mAb or isotype-control mAb was administered intraperitoneally on day-1, 0, 1, 3, and 5 post-MI/R. For inhibition of STAT3, 5 mg/kg STAT3 inhibitor (C188-9; S8605, Selleck Chem) or vehicle (DMSO) was administered intraperitoneally daily from 0 to 3 days after MI/R. For induction of the biIRI, both renal pedicles were clamped for 15 min. For two-stage uIRI, the left renal pedicle was clamped for 20 min on day 0, and the right kidney was removed on day14 (39). During the kidney procedures, mice were placed on a 43°C heat pad

Enzyme-linked immuno sorbent Assay (ELISA)

CTnI, NGAL, and HMGB-1 in the plasma were measured using cardiac Troponin-I ELISA kit (CTNI-1-HSP, Life Diagnostics), mouse NGAL ELISA kit (KE10045, Proteintech), and HMGB-1 ELISA kit II (326078738, Shino-Test Corporation), respectively, in accordance with the manufacturer's instructions. HMGB-1 ELISA kit is ensured no interference from >80% identical HMGB-2.

Infarct and ischemia area measurements

Twenty-four hours after MI/R, the heart was removed, and aortic cannulation was performed to inject 1 ml of saline to remove the remaining intracavitary blood. The LAD was re-ligated at the same location as in the ischemia induction, and then 0.5 ml of 1% Evans blue dye was injected into the aorta through the indwelling cannula to stain the non-ischemic area. Then, the heart was placed in an Eppendorf tube, frozen on dry ice, and sectioned into 1 mm short axis slices. The slices were incubated with 1% 2,3,5-triphenyl tetrazolium chloride (TTC) solution at 37℃ for 15min to stain viable myocardium as red and visualize the infarct area as white. The slices were fixed in 4% PFA at room temperature (RT). The non-ischemic area stained with Evans blue, the ischemic area stained with TTC (red area), and the infarct area (white area) were measured digitally using ImageJ software.

Tissue preparation for histology

Hearts and kidneys were fixed with 10 % formalin-buffered solution and embedded in paraffin. The heart and kidney slices with 3 μm-thick were stained by Masson's trichrome, periodic acid-Schiff (PAS), or Sirius-red, and analyzed using a digital BZ-X700 light and fluorescent microscope and BZ-X analysis software (Keyence). The percentage of fibrosis area was calculated as the ratio of fibrosis area to the whole ventricle wall or kidney in each section. To

analyze acute tubular necrosis (ATN) score in the kidney, the percent of tubules that displayed cell necrosis, loss of brush border, cast formation, and tubule dilatation were counted as follows: 0, none; 1, <10%; 2, 11% to 25%; 3, 26% to 45%; 4, 46% to 75%; and 5, >76%. For the fibrosis score, 10 fields in 200 times magnification were reviewed in each slide.

Immunohistochemistry

For multiplex immunohistochemistry (IHC), antibody staining and signal amplification were performed in accordance with the manufacturer's protocol (Opal 7-Color Manual IHC Kit, PerkinElmer) (40). Slide sections were incubated at RT for 1 h or at 4 °C overnight with primary antibodies in antibody diluent (Dako): CD31 (PECAM-1) (D8V9E) XP at 200x dilution (Cell Signaling Technology, #77699); anti-Vimentin antibody (Abcam, EPR3776) at 500x dilution (Abcam, ab92547); anti-alpha smooth muscle actin (αSMA) antibody at 100x dilution (Abcam, ab5694); anti-FSP-1/S100A4 antibody at 200x dilution (Sigma-Aldrich); anti-mouse Ly6G mAb (1A8) at 10,000x dilution (Bio X Cell, #BE0075-1); anti-kim-1 antibody at 200x dilution (R&D, AF1817); anti-p-H3 antibody at 200x dilution (Abcam, ab5176). Slides were washed twice with tris-buffered saline containing 0.05% Tween-20 (TBST) for 3 min and incubated with 2-3 drops of anti-mouse/rabbit Opal Polymer horseradish peroxidase (HRP) (ARH1001EA; PerkinElmer), or anti-rat IgG HRP-linked species-specific whole antibody (Cytiva, NA935) for 30 min at RT.. Tyramide signal amplification (TSA, PerkinElmer) was performed with the Opal 570 (Vimentin, CD31, and Kim-1), Opal 480 (FSP-1, Ly6G, and pH-3), or Opal 690 (αSMA) for 10 min at RT. Multiplex TSA experiments were performed by repeating staining cycles in series, with an antigen retrieval step each time and then counterstained with the nuclear counterstain 4, 6-diamidino-2-phenylindole (DAPI) (VectaShield, Vector Laboratories). Mantra Snap 1.0.3 (PerkinElmer) fluorescence microscope was used with epi-fluorescence filters of FITC, TRITC, Cy3, Texas Red, Cy5, and DAPI. Each OPAL fluorochrome and DAPI were

584 unmixed using mono fluorescence-stained slides, and multi-stained images were analyzed
585 with tissue segmentation, cell segmentation, and positive score by inForm Advanced Image
586 Analysis software (inForm 2.6, PerkinElmer). At least three fields at X20 magnification
587 containing ischemic area were analyzed for each sample. For the analysis of $CD31^+$ capillary
588 density, blinded quantification of $CD31^+$ capillaries was performed using the taken IHC
589 images with X20 magnification.
590
591 *Echocardiography*
592 Transthoracic echocardiography was performed using the Vevo 2100 imaging system
593 (Fujifilm Visual Sonics, Tokyo, Japan) under anesthesia with 1.5 % isoflurane. Long-axis B-
594 mode and M-mode images were used for measure of the echocardiography parameters,
595 including left ventricular (LV) end-diastolic dimension (LVDd) and end-systolic dimensions
596 (LVDs). The Teichholz formula [Volume = 7LVD3/(2.4+LVD)] was used to calculate the
597 LV end-diastolic volume (LVEDV) and LV end-systolic volume (LVESV). LV ejection
598 fraction (LVEF) and fractional shortening (LVFS), measures of LV systolic function, were
599 calculated using the following formula: LVEF (%) = (LVEDV - LVESV)/LVEDV × 100;
600 LVFS (%) = [(LVDd - LVDs)/LVDd] × 100.
601
602 *Cell preparation*
603 After mice were perfused with 20 ml PBS under deep anesthesia, their hearts and kidneys
604 were collected and minced with scissors into about 0.5 mm pieces in 5 mL of RPMI-1640
605 with 10% fetal bovine serum (FBS). The hearts were digested with Collagenase II (200
606 U/mL, Worthington Biochemical) and DNase I (60 U/ml, Worthington Biochemical) at 37°C
607 for 30 min with agitation on a rotator. Cells were separated using the gentleMACS
608 Dissociator (Miltenyi Biotech) according to the manufacturer's instruction and washed with

PBS supplemented with 1% FBS. The kidneys were digested using a tumor dissociation kit (Miltenyi Biotec) according to the manufacturer's instructions, followed by lysing erythrocytes using the ammonium chloride-potassium (ACK) lysis buffer (ThermoFisher). For the isolation of renal macrophages, renal cells were isolated with $CD11b^+$ microbeads (Miltenyi Biotec) using LS columns (Miltenyi Biotec). BM neutrophils were isolated by negative selection using the Neutrophil Isolation Kit (Miltenyi Biotec), as previously described (41). Human monocytes were purified from the peripheral blood with the EasySep Human Monocyte Isolation Kit (STEMCELL).

Antibodies and flow cytometry

Cells were incubated with Zombie NIR (BioLegend), Zombie violet (BioLegend) or propidium iodide to exclude dead cells and anti-mouse CD16/32 (clone 2.4G2, BD Biosciences) or a human FcR blocking reagent (Miltenyi) in a staining medium (PBS containing 2% FBS and 0.01% sodium azide) for 15 min to block the Fcγ receptors. Cells were then stained with the following antibodies for 30 min on ice. The fluorochrome-conjugated anti-mouse antibodies specific to CD45.2 (phycoerythrin (PE)-Cy7, clone 104), CD45.2 (BV421, clone 104), CD11b (BV711, clone M1/70), Ly6G (allophycocyanin; APC, clone 1A8), Ly6G (Fluorescein isothiocyanate; FITC, clone 1A8), Ly6C (PE, clone HK1.4), Ly6C (APC and Alexa Fluor 700, clone HK1.4) CD64 (BV605, clone X54-5/7.1), CD64 (PE, clone X54-5/7.1), CD11C (PE-Cy7, clone N418), I-A/I-E (BV510, clone M5/114.15.2), CD3e (FITC, clone 145-2C11), CD19 (FITC, clone 1D3/CD19), NK1.1 (FITC, clone PK136), BV421 Streptavidin and PE Streptavidin were purchased from BioLegend. Fluorochrome-conjugated anti-mouse antibodies specific to SiglecF (BV421 and PE, clone E50-2440), Gr-1 (PE, clone RB6-8C5), CD31 (Alexa Fluor 647, clone 390) and pSTAT3 (pY705, Alexa Fluor 488, clone 4/pSTAT3) were purchased from BD Biosciences and CD11b (APC Cy7, clone M1/70) was from TOMBO. Fluorochrome-conjugated anti-human antibodies specific to CD16 (PE, clone

3G8), CD56 (BV421, clone B159), CD19 (FITC, clone HIB19), CD4 (FITC, clone L200) and CD3 (PE, clone HIT3a) were purchased from BD Pharmingen, CD4 (V500, clone RPA-T4) was from BD Biosciences, CD14 (FITC and APC, clone Tuk4) was from Invitrogen and CD45 (BV421, clone 2D1) and CD8 (FITC, clone RPA-T8) were from Biolegend. Anti-mouse CD300a mAb (EX42) (29)and humanized anti-human CD300A mAb (TNAX103) (31)(32) were generated in our laboratory, as described previously (42). Recombinant human IgG1 (LALA-PG, N/A-CP149) was purchased from Bio X Cell.

All samples were analyzed by using the LSR Fortessa flow cytometer (Becton Dickinson) and FlowJo software (Tree Star). Doublets were excluded by gating out the population defined by forward scatter and side scatter in the flow cytometry in all the experiments. For pSTAT3 expression analysis, cells were fixed in Phosflow™ Lyse/Fix buffer (BD) for 10 min at 37°C and permeabilized with BD Phosflow™ Perm Buffer III for 30 min on ice before staining with anti-pSTAT3 (pY705) antibody.

Biochemical analysis

Plasma BUN and creatinine were measured using FUJI DRI-CHEM SLIDE BUN-PIII and CRE-PIII, respectively, according to the manufacturer's instructions.

Quantitative RT-PCR

Total RNA was extracted from renal cells 1, 5 and 7 days after biIRI or from neutrophils isolated from the heart 3 days after MIR using FACS Aria II (BD Biosciences). RNA was extracted using ISOGEN (Nippon Gene). cDNA was synthesized using a High-Capacity cDNA Reverse Transcription Kit (Applied Biosystems). Quantitative RT-PCR (qRT-PCR) was performed using Power SYBER Green PCR Master Mix (Applied Biosystem) and an ABI 7500 sequence detector (Applied Biosystems). Normalization of quantitative real-time PCR was performed based on the gene encoding β-actin. The sequences of primers are

shown, *β-actin* forward, 5'-ACTGTCGAGTCGCGTCCA 3'; *β-actin* reverse, 5'-GCAGCGATATCGTCATCCAT-3'; *Tgfb1* forward, 5'-TGACGTCACTGGAGTTGTACGG-3'; *Tgfb1* reverse, 5'-GGTTCATGTCATGGATGGTGC-3'; *Prok2* forward, 5'-GCCCCGCTACTGCTACTTC-3'; *Prok2* reverse, 5'-CCGCACTGAGAGTCCTTGTC-3'; *Chil1* forward, 5'-GTACAAGCTGGTCTGCTACTTC-3'; *Chil1* reverse, 5'-ATGTGCTAAGCATGTTGTCGC-3'; *Il1b* forward, 5'-ACTCAACTGTGAAATGCCACC-3'; *Il1b* reverse 5'-TGATACTGCCTGCCTGAAGC-3'; *Mmp9* forward, 5'-ACGACATAGACGGCATCCAGTATC-3'; *Mmp9* reverse 5'-AGGTATAGTGGGACACATAGTGGG-3'; *Il6* forward, 5'-AGTTGCCTTCTTGGGACTGA-3'; *Il6* reverse, 5'-TCCACGATTTCCCAGAGAAC-3'; *Tnf* forward, 5'-AGTTGCCTTCTTGGGACTGA-3'; *Tnf* reverse, 5'-TCCACGATTTCCCAGAGAAC-3'; *Ctgf* forward, 5′-GTGGAATATTGCCGGTGCA-3′; *Ctgf* reverse, 5 ′-CCATTGAAGCATCTTGGTTCG-3′.

Cytometric bead array analysis

To measure the amount of IL-1α, the plasma was collected from the coronary sinus at 6 hours after MI/R and analyzed by cytometric bead array according to the manufacturer's instructions (BD Biosciences) followed by CBA analysis FCAP software (BD Biosciences).

In vivo blocking of PS interaction with CD300a

D89E-MFG-E8 and the control protein (EPT-MFG-E8) (100 μg of each protein), which were generated as previously described (19), were administered intravenously 10 min before MI/R or biIRI.

RNA sequence

Single-cell suspension was prepared from the heart, and SiglecF^{hi} and SiglecF^{lo} neutrophils ($CD45.2^+$ $CD11b^+$ $Ly6G^+$) were isolated using FACS Aria II (BD Biosciences). In each experiment, more than 2×10^4 neutrophils from eight mice were pooled. RNA was extracted and purified using ISOGEN (Nippon Gene) and NEBNext Poly(A) mRNA Magnetic Isolation Module (New England Biolabs), respectively. Sequencing libraries of purified mRNA were prepared using the NEBNext Ultra II RNA Library Prep Kit (New England Biolabs). The synthesized libraries were checked for yield using Agilent High Sensitivity DNA Kit (Agilent Technologies). The libraries were sequenced with Illumina NextSeq500/550 v2.5 Kit (#20024906, Illumina) for 75 cycles to obtain more than 20 million reads as paired-end reads in each sample. CLC Genomics Workbench 20.0 software (QIAGEN, Hilden, Germany) was used to calculate transcripts per million (TPM) and fold change and to generate principal component analysis. The genes with TPM of more than 10 were used in the analysis. Heatmapper (http:// www.heatmapper.ca/) was used to make the heat map; R was used to make the Volcano plot. Gene ontology analysis (Biological processes) of DEG was performed using DAVID (v2023q2). Gene set enrichment analysis (GSEA) was performed using GSEA version 4.3.2. RNA sequence analysis of healthy and CKD kidneys was performed using the Nephroseq database (www. nephroseq. org.University of Michigan, Ann Arbor, MI, USA).

Preparation of the supernatant from cardiac tissue

The hearts were collected, and the luminal blood was washed out with RPMI-1640 with 10% FBS. The hearts were then crushed with frosted edge glass slides, stimulated or not with HMGB1 (1 μg/ml) or IL-1α (10 ng/ml) for 6 h. and the supernatant was collected.

Adoptive transfer of neutrophils

712 BM-derived neutrophils (1×10^6 cells) from WT or *Cd300a*$^{-/-}$ mice were intravenously injected
713 into WT mice on days 0 and 3 after MI/R as previously described (12). Cardiac tissue was
714 collected on day 7 after MI/R to perform immunohistochemical analysis.
715
716 *Bone marrow (BM) chimeric mice*
717 BM chimeric mice were generated as described previously (19). In brief, R26GRR mice at 4
718 to 5 weeks old were irradiated with 5 Gy two times. BM cells (1×10^7) from td*Tomato*$^{fl/fl}$*Lyz2*-
719 Cre, *Cd300a*$^{fl/fl}$td*Tomato*$^{fl/fl}$*Lyz2*-Cre, wild-type, or *Cd300b*$^{-/-}$ mice were injected into the tail
720 veins of irradiated recipients immediately after the final irradiation. Four weeks after BM cell
721 transfer, these mice were subjected to renal ischemia and reperfusion.
722
723 *Efferocytosis assay*
724 Dead Jurkat cells were generated by using 1μM staurosporine (Wako Fujifilm) and stained
725 with 100ng/mL pHrodo-SE (Invitrogen) for 30 min at RT. Human monocytes (2×10^5) were
726 incubated with anti-human CD300A mAbs (10 μg/ml) for 120 min at 37 ˚C and cocultured
727 with dead Jurkat cells (4×10^5) for 120 min at 37 ˚C. Efferocytosis was analyzed by confocal
728 laser scanning microscopy (Fluoview FV10i, Olympus). Digital images of randomly selected
729 fields under confocal microscopy were captured, and more than 100 cells that engulfed dead
730 cells were analyzed. The phagocytic index was calculated according to the following formula
731 (43): phagocytic index = (total number of engulfed cells/total number of counted macrophages)
732 × (number of macrophages containing engulfed cells/total number of counted macrophages) ×
733 100.
734
735 *Statistics*

Statistical analyses were performed by using GraphPad Prism 9 or 10 (GraphPad Software). Results are presented as means ± SEM. *P*-values less than 0.05 were considered statistically significant. The unpaired or paired Student's *t*-test (two-tailed) or one- or two-way ANOVA tests were performed to compare more than two groups. Where applicable, post hoc multiple comparison tests were performed (Tukey for pairs, Bonferroni for multiple groups).

Study approval

All animal experiments were approved by the University of Tsukuba Animal Resource Center (approved number: 23-332) and performed in accordance with the guidelines of the animal ethics committee of the University of Tsukuba Animal Resource Center (Tsukuba, Japan).

Data availability

The RNA-seq data have been deposited at GEO (GSE263749) and are publicly available as of the date of publication. All data generated in this study are available in the Supporting Data Values file.

Author contributions

C. N-O. and A. S. conceptualized the study. N.N., H. K., C. N-O., S. F., X. N., H. L., F. A., J. L. and Y. X. conducted the investigation. N.N., H. K., S. F., F. A., J. L. and K. T. performed animal studies. N. N., H. K., C. N-O., X. N., H. L. and T. S. performed visualization. T. S. and M. I. contributed to methodology. N.N., H. K. and C. N-O. wrote the manuscript. C. N-O., K. T., K. S., and A. S. reviewed and edited the manuscript. C. N-O. and A. S. supervised and acquired funding for the study.

Acknowledgments

A. S. was funded by the JSPS KAKENHI (21H04836). C. N-O. was funded by the JSPS KAKENHI (22H03170) and Takeda Science Foundation. The authors thank H. Furugen and M. Kaneko for administrative support.

REFERENCES

1. Dick SA, Epelman S. Chronic Heart Failure and Inflammation: What Do We Really Know? *Circ Res*. 2016;119(1):159–176.
2. Kellum JA, et al. Acute kidney injury. *Nat Rev Dis Primers*. 2021;7(1):52.
3. Rangaswami J, et al. Cardiorenal Syndrome: Classification, Pathophysiology, Diagnosis, and Treatment Strategies: A Scientific Statement From the American Heart Association. *Circulation*. 2019;139(16).
4. Ronco C, Bellomo R, Kellum JA. Acute kidney injury. *The Lancet*. 2019;394(10212):1949–1964.
5. Webster AC, et al. Chronic Kidney Disease. *The Lancet*. 2017;389(10075):1238–1252.
6. Rosin DL, Okusa MD. Dangers Within: DAMP Responses to Damage and Cell Death in Kidney Disease. *Journal of the American Society of Nephrology*. 2011;22(3):416–425.
7. Huang Y, Jiang W, Zhou R. DAMP sensing and sterile inflammation: intracellular, intercellular and inter-organ pathways. *Nat Rev Immunol*. 2024;24(10):703–719.
8. Eming SA, Wynn TA, Martin P. Inflammation and metabolism in tissue repair and regeneration. *Science*. 2017;356(6342):1026–1030.
9. Calcagno DM, et al. SiglecF(HI) Marks Late‐Stage Neutrophils of the Infarcted Heart: A Single‐Cell Transcriptomic Analysis of Neutrophil Diversification. *Journal of the American Heart Association*. 2021;10(4):e019019.
10. Vafadarnejad E, et al. Dynamics of Cardiac Neutrophil Diversity in Murine Myocardial Infarction. *Circ Res*. 2020;127(9). https://doi.org/10.1161/CIRCRESAHA.120.317200.
11. Shin JW, et al. A unique population of neutrophils generated by air pollutant–induced lung damage exacerbates airway inflammation. *Journal of Allergy and Clinical Immunology*. 2022;149(4):1253-1269.e8.
12. Ryu S, et al. Siglec-F–expressing neutrophils are essential for creating a profibrotic microenvironment in renal fibrosis. *Journal of Clinical Investigation*. 2022;132(12):e156876.
13. Borrego F. The CD300 molecules: an emerging family of regulators of the immune system. *Blood*. 2013;121(11):1951–1960.
14. Yotsumoto K, et al. Paired Activating and Inhibitory Immunoglobulin-like Receptors, MAIR-I and MAIR-II, Regulate Mast Cell and Macrophage Activation. *Journal of Experimental Medicine*. 2003;198(2):223–233.
15. Shibuya A, Nakahashi-Oda C, Tahara-Hanaoka S. Regulation of Immune Responses by the Activating and Inhibitory Myeloid-Associate Immunoglobuline-Like Receptors (MAIR) (CD300). *Immune Netw*. 2009;9(2):41.
16. Nakahashi-Oda C, et al. Identification of phosphatidylserine as a ligand for the CD300a immunoreceptor. *Biochemical and Biophysical Research Communications*. 2012;417(1):646–650.
17. Nakahashi-Oda C, et al. Apoptotic cells suppress mast cell inflammatory responses via the CD300a immunoreceptor. *Journal of Experimental Medicine*. 2012;209(8):1493–1503.
18. Nakahashi-Oda C, et al. Apoptotic epithelial cells control the abundance of Treg cells at barrier surfaces. *Nat Immunol*. 2016;17(4):441–450.
19. Nakahashi-Oda C, et al. CD300a blockade enhances efferocytosis by infiltrating myeloid cells and ameliorates neuronal deficit after ischemic stroke. *Sci Immunol*. 2021;6(64):eabe7915.
20. Saraswati S, et al. Identification of a pro-angiogenic functional role for FSP1-positive fibroblast subtype in wound healing. *Nat Commun*. 2019;10(1):3027.
21. Singer E, et al. Neutrophil gelatinase‐associated lipocalin: pathophysiology and clinical applications. *Acta Physiologica*. 2013;207(4):663–672.
22. Ferenbach DA, Bonventre JV. Mechanisms of maladaptive repair after AKI leading to accelerated kidney ageing and CKD. *Nat Rev Nephrol*. 2015;11(5):264–276.

817 23. Chevalier RL, Forbes MS, Thornhill BA. Ureteral obstruction as a model of renal
818 interstitial fibrosis and obstructive nephropathy. *Kidney International*. 2009;75(11):1145–
819 1152.
820 24. Hanayama R, et al. Identification of a factor that links apoptotic cells to phagocytes.
821 *Nature*. 2002;417(6885):182–187.
822 25. Noel JG, et al. IL-1/MyD88–Dependent G-CSF and IL-6 Secretion Mediates Postburn
823 Anemia. *The Journal of Immunology*. 2023;210(7):972–980.
824 26. Leizer T, Cebon J. Cytokine Regulation of Colony-Stimulating Factor Production in
825 Cultured Human Synovial Fibroblasts: I. Induction of GM-CSF and G-CSF Production by
826 Interleukin-1 and Tumor Necrosis Factor.
827 27. Yan B, et al. IL-6 Cooperates with G-CSF To Induce Protumor Function of Neutrophils
828 in Bone Marrow by Enhancing STAT3 Activation. *The Journal of Immunology*.
829 2013;190(11):5882–5893.
830 28. Itatani Y, et al. Suppressing neutrophil-dependent angiogenesis abrogates resistance to
831 anti-VEGF antibody in a genetic model of colorectal cancer. *Proceedings of the National*
832 *Academy of Sciences*. 2020;117(35):21598–21608.
833 29. Wang Y, et al. Autonomous regulation of IgE-mediated mast cell degranulation and
834 immediate hypersensitivity reaction by an inhibitory receptor CD300a. *Journal of Allergy*
835 *and Clinical Immunology*. 2019;144(1):323-327.e7.
836 30. Ieda M, et al. Direct Reprogramming of Fibroblasts into Functional Cardiomyocytes by
837 Defined Factors. *Cell*. 2010;142(3):375–386.
838 31. Koizumi H, et al. Development of Monoclonal Antibodies Specific to Either CD300A^{R111}
839 or CD300A^{Q111} or Both. *Monoclonal Antibodies in Immunodiagnosis and Immunotherapy*.
840 2023;42(5):182–185.
841 32. Abe F, et al. A Humanized Monoclonal Antibody Against CD300A Ameliorates Acute
842 Ischemic Stroke in Humanized Mice. *Monoclonal Antibodies in Immunodiagnosis and*
843 *Immunotherapy*. 2025;44(1):2–7.
844 33. Pfirschke C, et al. Tumor-Promoting Ly-6G+ SiglecFhigh Cells Are Mature and Long-
845 Lived Neutrophils. *Cell Rep*. 2020;32(12):108164.
846 34. Taguchi K, et al. Cyclin G1 induces maladaptive proximal tubule cell dedifferentiation
847 and renal fibrosis through CDK5 activation. *Journal of Clinical Investigation*.
848 2022;132(23):e158096.
849 35. Zhang Y, et al. HDAC9-mediated epithelial cell cycle arrest in G2/M contributes to
850 kidney fibrosis in male mice. *Nat Commun*. 2023;14(1):3007.
851 36. Hasegawa Y, et al. Novel ROSA26 Cre-reporter Knock-in C57BL/6N Mice Exhibiting
852 Green Emission before and Red Emission after Cre-mediated Recombination. *Exp Anim*.
853 2013;62(4):295–304.
854 37. Madisen L, et al. A robust and high-throughput Cre reporting and characterization system
855 for the whole mouse brain. *Nat Neurosci*. 2010;13(1):133–140.
856 38. Xu Z, et al. A Murine Model of Myocardial Ischemia-reperfusion Injury through Ligation
857 of the Left Anterior Descending Artery. *JoVE*. 2014;(86):51329.
858 39. Wei J, et al. New mouse model of chronic kidney disease transitioned from ischemic
859 acute kidney injury. *American Journal of Physiology-Renal Physiology*. 2019;317(2):F286–
860 F295.
861 40. Pivetta E, et al. Multiplex staining depicts the immune infiltrate in colitis-induced colon
862 cancer model. *Sci Rep*. 2019;9(1):12645.
863 41. McGill CJ, Lu RJ, Benayoun BA. Protocol for analysis of mouse neutrophil NETosis by
864 flow cytometry. *STAR Protocols*. 2021;2(4):100948.
865 42. Yamashita-Kanemaru Y, et al. Suppression of Th1 and Th17 Proinflammatory Cytokines
866 and Upregulation of FOXP3 Expression by a Humanized Anti-DNAM-1 Monoclonal

867 Antibody. *Monoclonal Antibodies in Immunodiagnosis and Immunotherapy*. 2021;40(2):52–
868 59.
869 43. Sano H, et al. Critical role of galectin-3 in phagocytosis by macrophages. *J Clin Invest*.
870 2003;112(3):389–397.
871
872

Figure legends

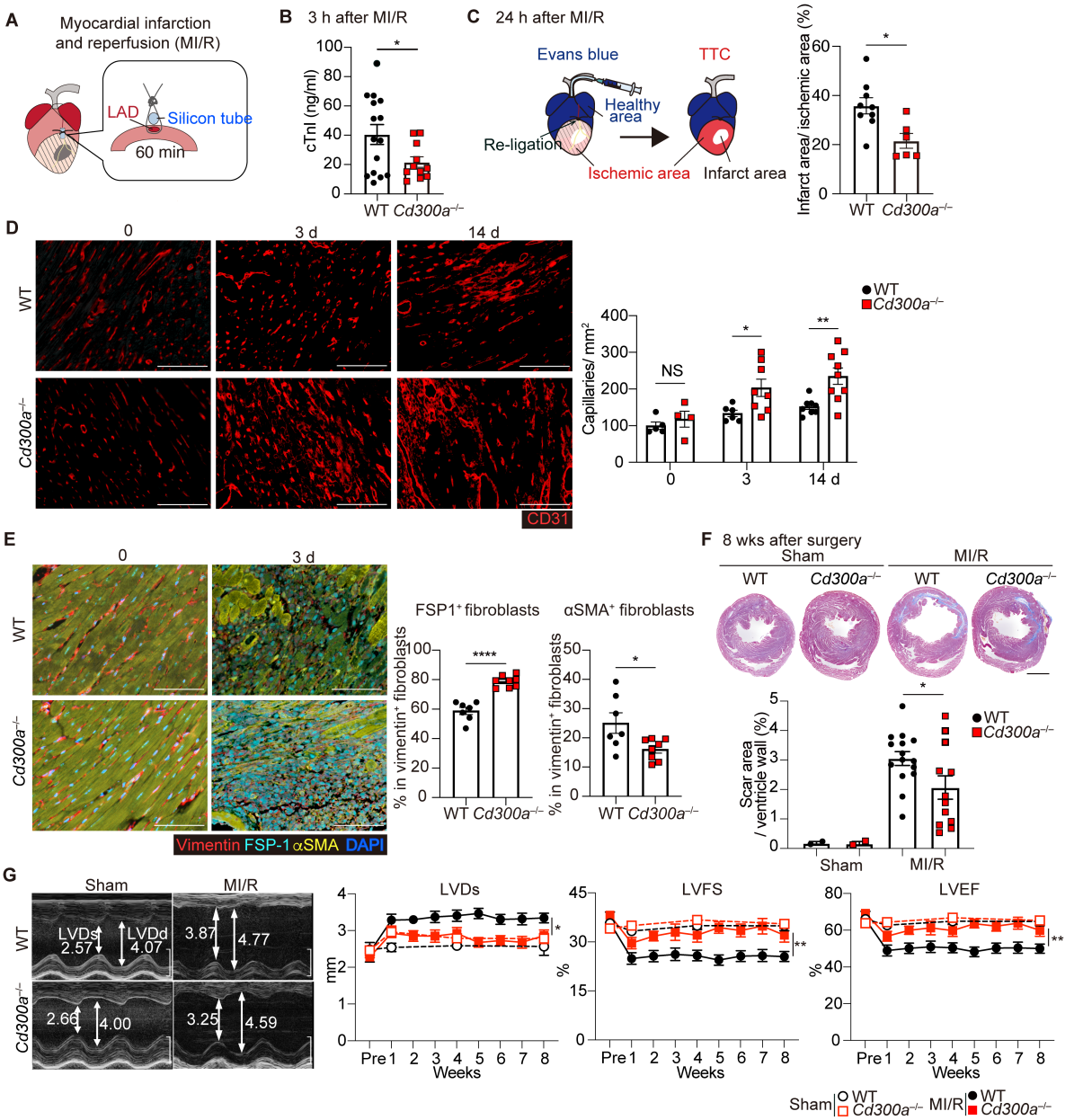

Figure 1. CD300a deletion ameliorates myocardial ischemia and reperfusion injury and adverse remodeling.
(A) MI/R model. **(B)** Plasma cTnI in *Cd300a*$^{-/-}$ (n = 11) and WT mice (n = 15). **(C)** Evans blue and TTC staining (left) and the percentage of infarct area among ischemic area in *Cd300a*$^{-/-}$ (n = 6) and WT mice (n = 9). **(D)** Representative immunohistochemistry (left) and quantitative data of CD31^{+} capillary density in peri-infarct area in *Cd300a*$^{-/-}$ (n = 4 (day 0), 8 (3) and 9 (14)) and WT mice (n = 5 (day 0), 6 (3) and 8 (14)). Scale bars, 100 μm. **(E)** Representative immunohistochemistry (left) and the percentage of FSP1^{+} and αSMA^{+} fibroblast in vimentin^{+} fibroblast in infarct area in *Cd300a*$^{-/-}$ (n = 8) and WT mice (n = 7). Scale bars, 100 μm. **(F)** Representative Masson's trichrome staining of the heart (left). Fibrosis area in *Cd300a*$^{-/-}$ (n = 12 in MI/R and n = 2 in sham) and WT heart (n = 15 in MI/R and n = 2 in sham). Scale bar, 1 mm. **(G)** Representative echocardiography images (left) and left ventricular internal dimension in systole (LVDs), fractional shortening (LVFS) and ejection fraction (LVEF) (n = 2 in each group) in *Cd300a*$^{-/-}$ mice (n = 12) and WT mice (n =

15). Scale bars, 2 mm. Data are presented as means ± SEM and pooled from more than 5 (B, C, F, and G) and 3 experiments (D and E). Dots represent independent animals. Statistical analysis was performed using unpaired Student's *t*-test (B, C, and E) and two-way ANOVA (D, F, and G). *, $P < 0.05$; **, $P < 0.01$; ****, $P < 0.0001$; NS, not significant.

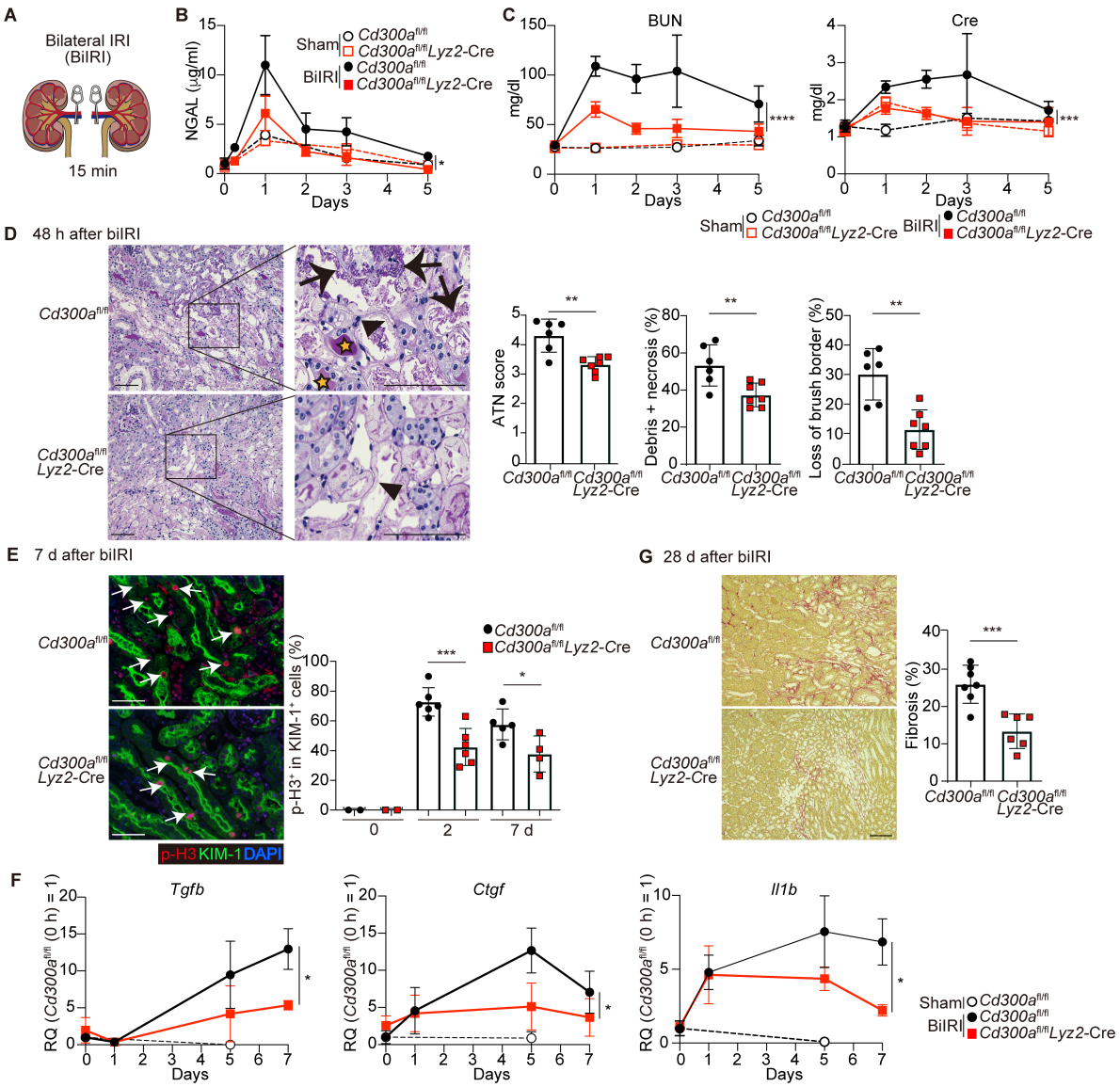

Figure 2. CD300a-deficiency ameliorates acute kidney injury and fibrosis after biIRI. (**A**) Bilateral ischemia-reperfusion injury model (biIRI). (**B**) Plasma NGAL in sham operation (n = 4 in each group) and after biIRI (*Cd300a*$^{fl/fl}$ mice, n = 3 (0 h), 4 (6 h), 13 (day 1), 7 (2), 6 (3) and 4 (5); *Cd300a*$^{fl/fl}$*Lyz2*-Cre mice, n = 3 (0 h), 4 (6 h), 13 (day 1), 6 (2), 4 (3), and 4 (5)). (**C**) Plasma BUN and Cre in sham (n = 4) and after biIRI (n = 5 (day 0), 31(1), 24 (2), 9 (3), and 9 (5)) in each group. (**D**) Representative PAS staining of kidneys after biIRI in *Cd300a*$^{fl/fl}$ and *Cd300a*$^{fl/fl}$*Lyz2*-Cre mice (n = 6 or 7). Arrow, loss of brush border; arrowhead, necrosis; star, debris. (**E**) Representative KIM-1 and p-H3 staining of kidneys after biIRI (left). The percentage of p-H3^{+} cells in KIM-1^{+} cells of *Cd300a*$^{fl/fl}$ (n = 2 (0), 6 (2 d) and 5 (7 d)) and *Cd300a*$^{fl/fl}$ *Lyz2*-Cre mice (n=2, 6, and 4). (**F**) *Tgfb*, *Ctgf* and *Il1b* mRNA expressions in the kidneys in sham (n = 2) and after biIRI (n = 3 (days 0, 1, and 5) and 5 (7) in each group) (**G**) Representative Sirius-red staining of kidneys after biIRI (left). Fibrosis in tubulointerstitial area in *Cd300a*$^{fl/fl}$ and *Cd300a*$^{fl/fl}$ *Lyz2*-Cre mice (n =7 or 5). Scale bars, 100 μm (D, E, and G). Data are presented as means ± SEM and pooled of 2 (B, D, F, and G), 3 (E), and 5 (C) experiments. Statistical analyses were performed using unpaired Student's *t*-test (B–D, F and G) and two-way ANOVA (E). *, $P < 0.05$; **, $P < 0.01$; ***, $P < 0.001$; ****, $P < 0.0001$.

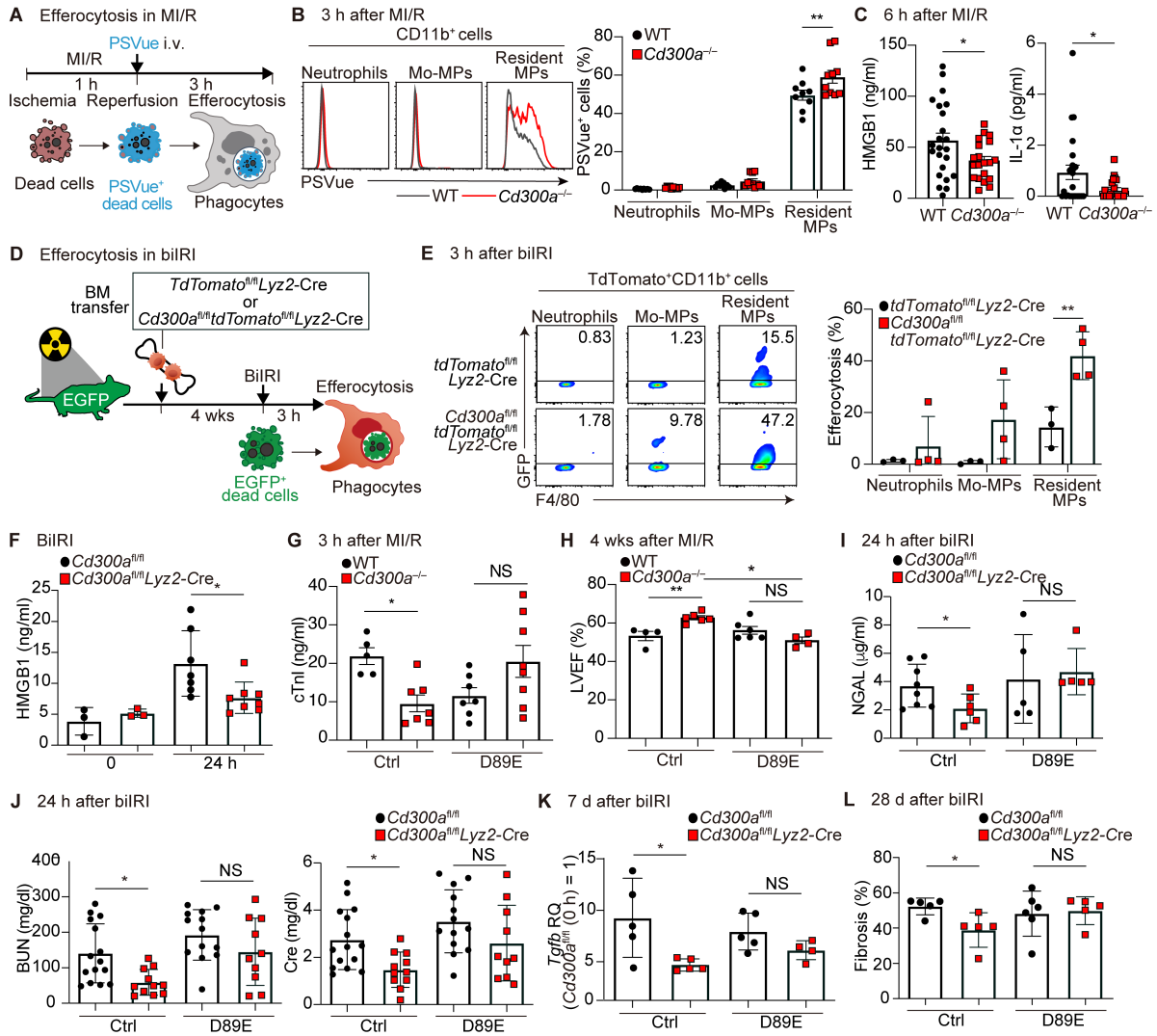

Figure 3. Enhanced efferocytosis reduces tissue damage and fibrosis and preserves organ function after MI/R and bilRI.

(**A, B**) Efferocytosis of PSVue$^+$ cells by CD11b$^+$ myeloid cells in the heart of *Cd300a*$^{-/-}$ (n = 10) and WT mice (n = 9). (**C**) Plasma HMGB1 and IL-1α in *Cd300a*$^{-/-}$ and WT mice (n = 23 or 24 in each group). (**D, E**) Efferocytosis of host-derived EGFP$^+$ dead cells by donor-derived tdTomato$^+$CD11b$^+$ myeloid cells in the tdTomato-GFP chimeric mouse kidneys (n = 3 or 4 in each group). (**F**) Plasma HMGB1 in *Cd300a*$^{fl/fl}$ and *Cd300a*$^{fl/fl}$ *Lyz2*-Cre mice (n = 3 (0 h) and 7 or 8 (24 h)). (**G, H**) Plasma cTnI and LVEF in Ctrl or D89E-administered *Cd300a*$^{-/-}$ mice (Ctrl, n = 7 or 6; D89E, n = 8 or 4) and WT mice (Ctrl, n = 5 or 4; D89E, n = 7 or 6). (**I** and **J**) Plasma NGAL and BUN and Cre in ctrl or D89E-administered *Cd300a*$^{fl/fl}$ (n = 8 or 5 for (I) and n = 15 or 14 for (J)) and *Cd300a*$^{fl/fl}$*Lyz2*-Cre mice (n = 6 or 5 for (I) and n = 11 or 10 for (J)). (**K, L**) *Tgfb* expression and the fibrosis area by Masson's trichrome staining in the kidneys of ctrl or D89E-administered *Cd300a*$^{fl/fl}$ (n = 5 in each group for (K) and n = 5 or 6 for (L)) and *Cd300a*$^{fl/fl}$*Lyz2*-Cre (n = 5 or 4 for (K) and n = 5 in each group for (L)) mice. Means ± SEM and pooled of 2 (E, I, K, and L), 3 (B, C, F–H), and 5 (J) experiments. Two-way ANOVA (B, E–L) and unpaired Student's *t*-test (C). *, $P < 0.05$; **, $P < 0.01$; NS, not significant.

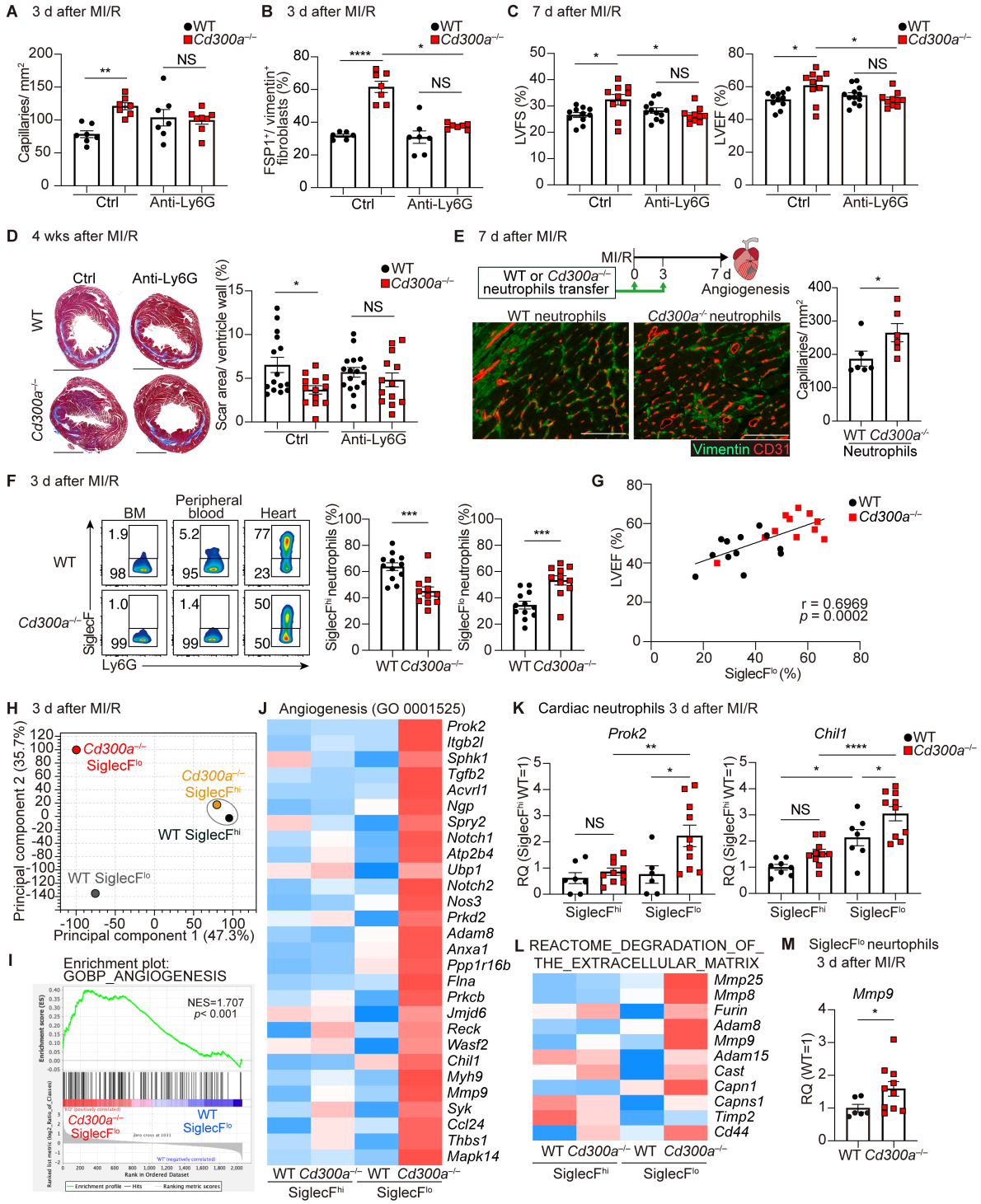

Figure 4. CD300a-deficiency upregulates pro-angiogenic and anti-fibrotic genes in SiglecF^{lo} neutrophils.

(**A-D**) CD31^{+} capillary density in peri-infarct area (A), the percentage of FSP1^{+} cells (B), LVFS and LVEF (C), and the percentage of scar areas (D) in isotype-control (Ctrl) or anti-Ly6G mAb-administered *Cd300a*$^{-/-}$and WT mice (Ctrl, n =6~8 (A, B), 10~12 (C), and 13 =16 (D)). (**E**) CD31^{+} capillary density in the peri-infarct area in the heart of mice transferred with WT or *Cd300a*$^{-/-}$ neutrophils. Scale bar: 100 μm. (**F**) Flow cytometric analysis of SiglecF^{hi} and SiglecF^{lo} neutrophils in the cardiac tissue in WT (n = 12) and *Cd300a*$^{-/-}$ (n = 11) mice. (**G**) The correlation between LVEF and the percentages of SiglecF^{lo} neutrophils.

(**H**) PCA plot of RNA expressions of SiglecF^{hi} and SiglecF^{lo} neutrophils in the cardiac tissue from WT and *Cd300a*$^{-/-}$ mice (n = 8 in each group). (**I**) GSEA profiles of enrichment gene sets associated with angiogenesis in *Cd300a*$^{-/-}$ and WT SiglecF^{lo} neutrophils. (**J**) Heat map of enriched genes associated with angiogenesis. (**K**) *Prok2* and *Chil1* mRNA expressions in SiglecF^{hi} and SiglecF^{lo} neutrophils in cardiac tissue in *Cd300a*$^{-/-}$and WT mice (n = 10 or 7). (**L**) Heat map of enriched genes associated with degradation of the extracellular matrix. (**M**) *Mmp9* mRNA expression in SiglecF^{lo} neutrophils in the cardiac tissue in *Cd300a*$^{-/-}$ and WT mice (n = 7 or 10). Scale bars: 1 mm (D) and 100 μm (E). Means ± SEM and pooled from 2 (E–G) and more than 5 (A–D, K, and M) experiments. Two-way ANOVA (A–D and K) and unpaired Student's *t*-test (E, F, and M). *, $P < 0.05$; **, $P < 0.01$; ***, $P < 0.001$; ****, $P < 0.0001$; NS, not significant.

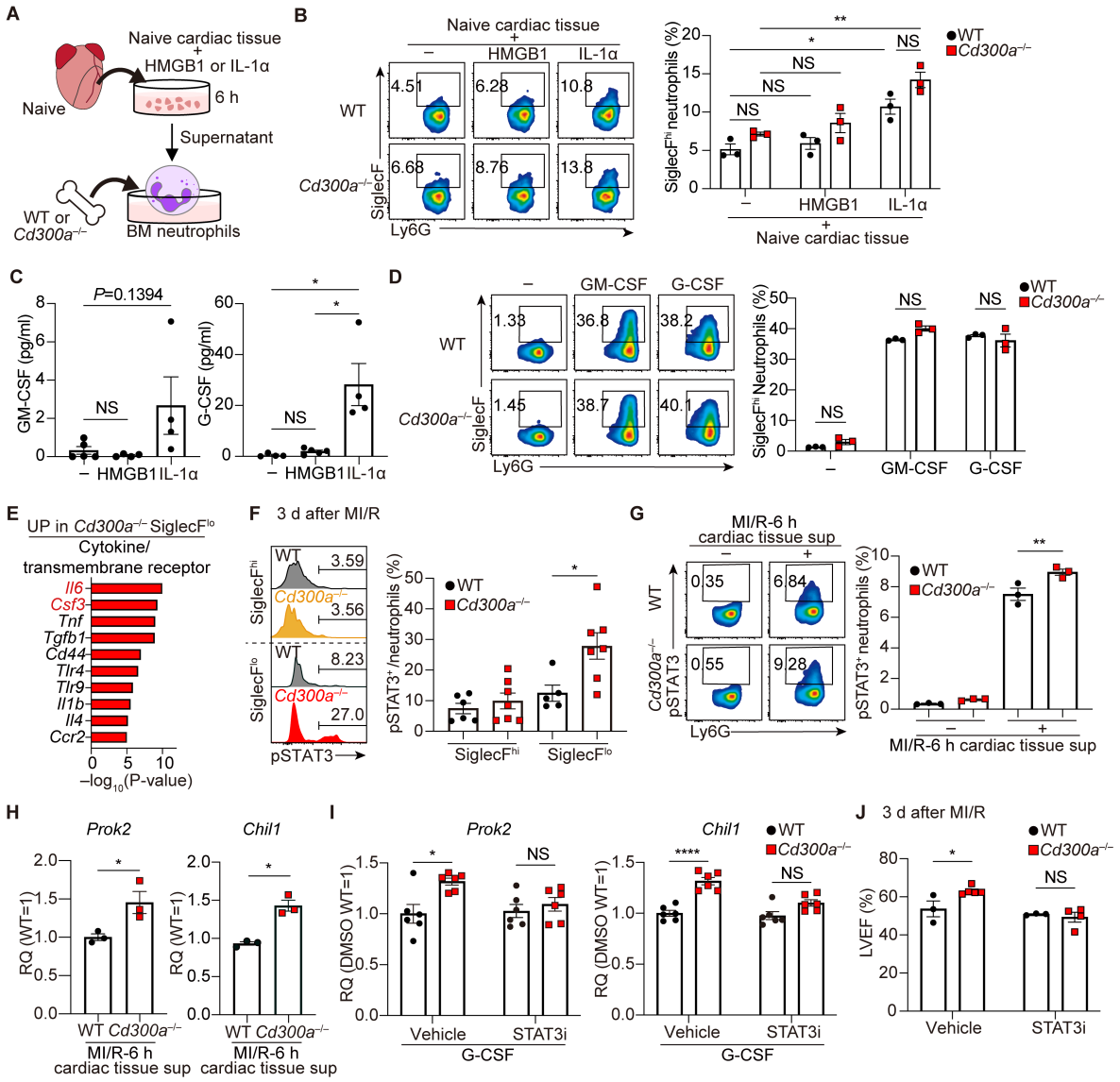

Figure 5. CD300a suppresses STAT3 phosphorylation in SiglecF^{lo} neutrophils.
(**A**–**C**) WT or *Cd300a*$^{-/-}$ BM neutrophils were cultured for 2 d in the presence of the culture supernatant of the naïve cardiac tissue, which had been stimulated or not with HMGB1 or IL-1α (A) and analyzed for SiglecF expression by flow cytometry (B). The GM-CSF and G-CSF levels in the culture supernatant of the cardiac tissue after stimulation with HMGB-1 or IL-1α (C). (**D**) Flow cytometric analysis of SiglecF expression on WT or *Cd300a*$^{-/-}$ BM neutrophils after stimulation with GM-CSF or G-CSF. (**E**) Ingenuity pathway analysis (IPA) based on DEGs from *Cd300a*$^{-/-}$ and WT SiglecF^{lo} neutrophils. (**F** and **G**) Flow cytometric analysis of phosphorylated STAT3 (pSTAT3) in neutrophils of the cardiac tissue of *Cd300a*$^{-/-}$ (n = 7) and WT (n = 6) mice (F) and WT or *Cd300a*$^{-/-}$ BM neutrophils stimulated with or without the cardiac tissue supernatant (G). (**H** and **I**) *Prok2* and *Chil1* mRNA expression in BM neutrophils of WT or *Cd300a*$^{-/-}$ mice stimulated with the cardiac tissue supernatant after MI/R (H) or with G-CSF together with STAT3 inhibitor (STAT3i) or control vehicle (Vehicle) (I). (**J**) LVEF after MI/R in *Cd300a*$^{-/-}$ (Vehicle n = 5; STAT3i n = 4) and WT mice (n = 3 in each group) treated with STAT3i or vehicle. Means ± SEM, representative of 2 experiments (B, D, G, and H) and pooled from 2 (C, F, and I) and 4 (J) experiments. One-

975 way (B, C, and D) and two-way ANOVA (F, G, I, and J), and unpaired Student's *t*-test (H).
976 *, $P < 0.05$; **, $P < 0.01$; ***, $P < 0.001$; ****, $P < 0.0001$. NS, not significant.
977

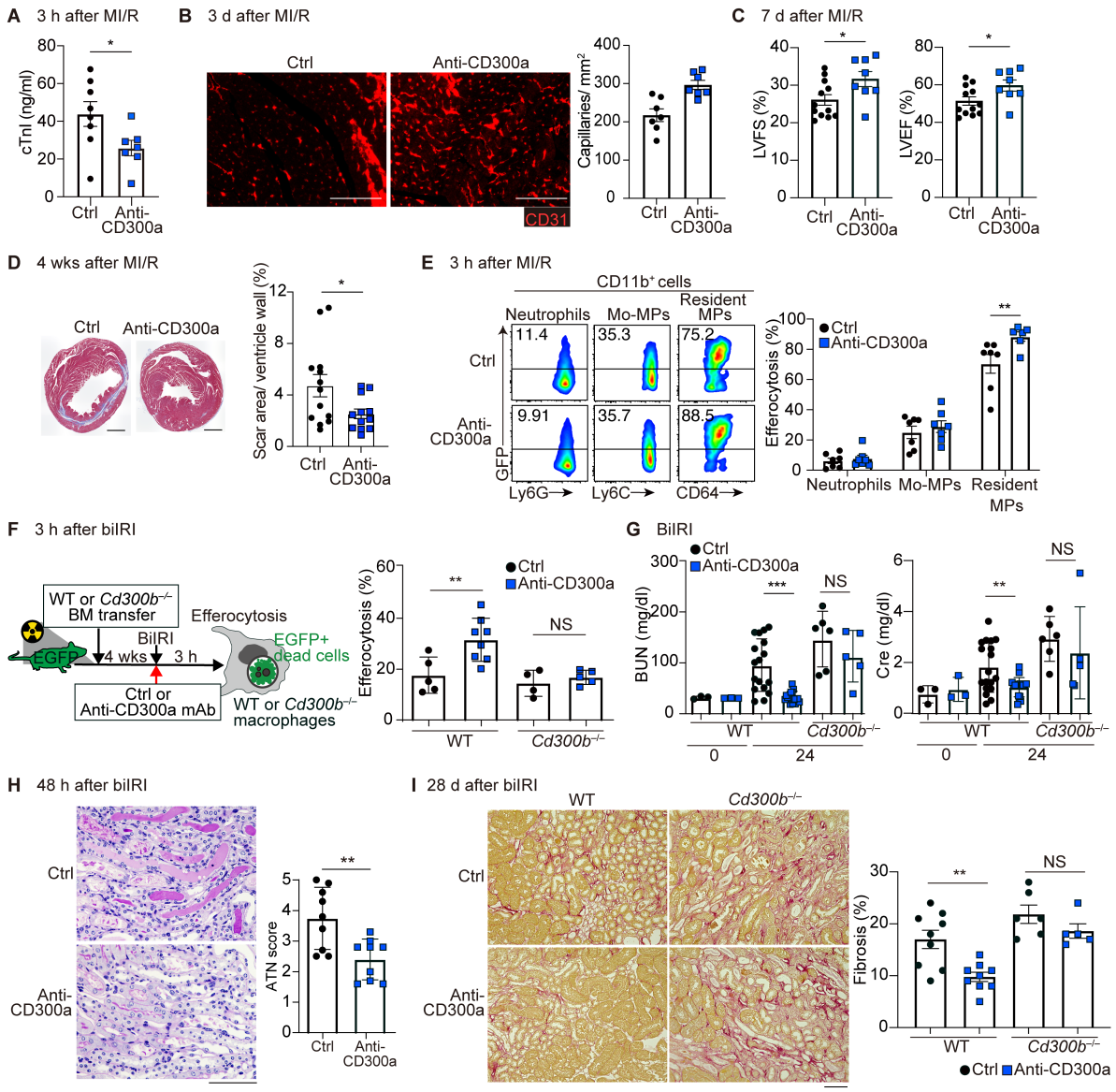

Figure 6. Anti-CD300a mAb ameliorated tissue injury and adverse remodeling.
(A) Plasma cTnI in anti-CD300a mAb or Ctrl-administered mice (n = 7 or 8). **(B)** CD31$^+$ capillary density in peri-infarct area in anti-CD300a mAb or Ctrl-administered mice (n = 7). **(C)** LVFS and LVEF in anti-CD300a mAb or Ctrl-administered mice (n = 7 or 5). **(D)** Masson's trichrome staining and the fibrosis area in the ventricle in anti-CD300a mAb or Ctrl-administered mice (n = 10 or 11). **(E)** Efferocytosis of GFP$^+$ dead cells by myeloid cell subpopulations in the cardiac tissue of αMHC-GFP mice administered with anti-CD300a mAb or Ctrl (n = 6 or 7). **(F)** Generation of BM chimeric R26GRR mice (GFP$^+$ mice) and efferocytosis of host-derived GFP$^+$ dead cells by resident macrophages of the chimeric mice administered with an anti-CD300a mAb (n = 8 or 5) or Ctrl (n = 5 or 4). **(G)** Plasma BUN and Cre in WT and *Cd300b*$^{-/-}$ mice administered with anti-CD300a mAb or Ctrl (WT; n = 3 or 17, *Cd300b*$^{-/-}$; n = 5 or 6). **(H)** PAS staining of the kidney and ATN score in mice administered with anti-CD300a mAb or Ctrl (n = 9 in each group). **(I)** Sirius-red staining and the fibrosis area in WT and *Cd300b*$^{-/-}$ mice administered with anti-CD300a mAb or Ctrl (WT; n = 8, *Cd300b*$^{-/-}$; n = 5 or 6). Scale bars: 100 μm (B, H, and I) and 1 mm (D). Means ± SEM and pooled from 2 (A–D, F, H, and I) and 5 (E and G) experiments. Student's *t*-test (A–D and H) and two-way ANOVA (E–G and I). *, $P < 0.05$; **, $P < 0.01$; ***, $P < 0.001$.

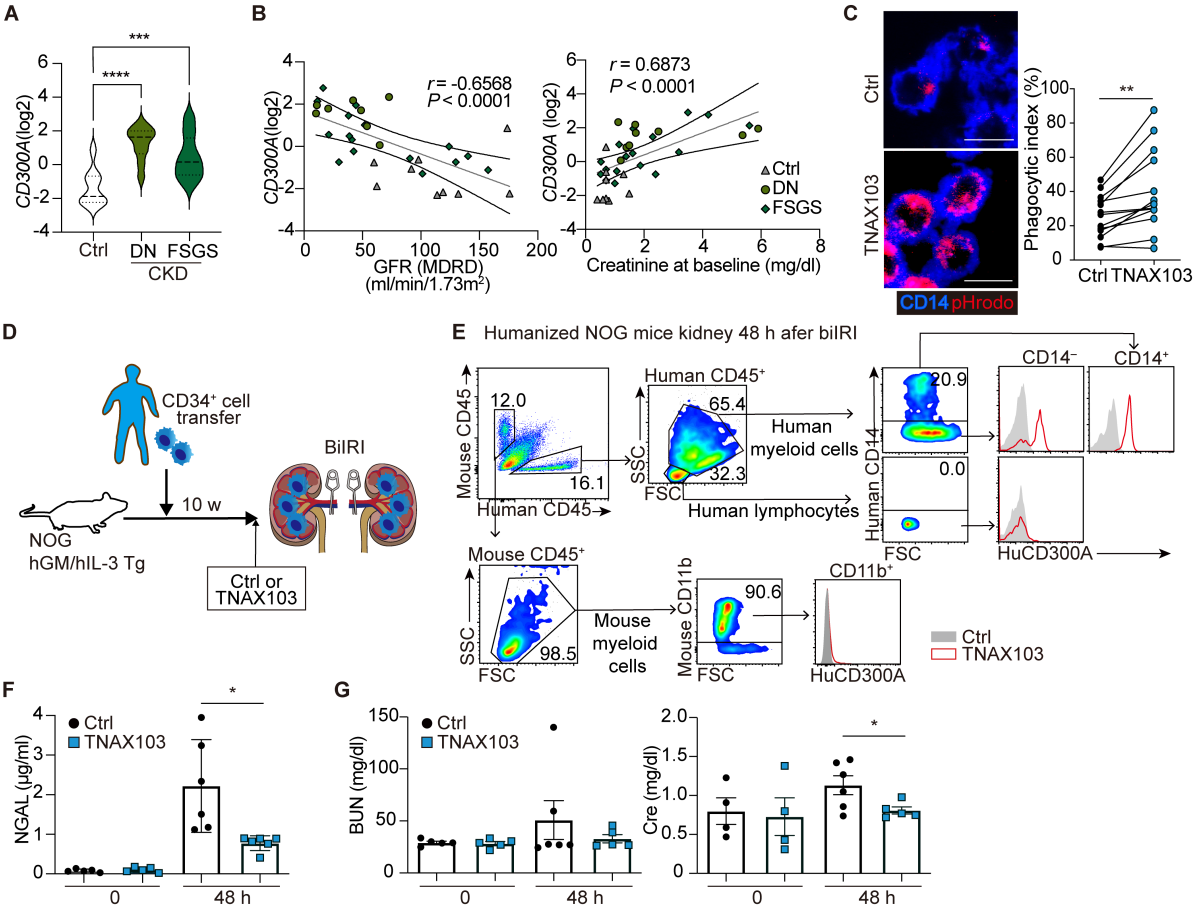

Figure 7. Blockade of human CD300A enhanced efferocytosis and ameliorated acute renal injury after biIRI.

(**A** and **B**) A public gene expression data set of patients with CKD of diabetic nephropathy (DN) (n = 9) and focal segmental glomerulosclerosis (FSGS) (n = 19). *CD300A* expression compared with the healthy control (HC) group (n = 10) (A) and Spearman correlation analysis between the expression of *CD300A* and renal function of glomerular filtration rate (GFR) and creatinine (B). (**C**) Efferocytosis of pHrodo-labeled dead Jurkat cells by human monocytes from 13 donors in the presence of control mAb (Ctrl) and a humanized anti-CD300A mAb (TNAX103). Representative laser scanning confocal microscopy image (left) and phagocytic index (right). (**D**) Schematic diagram of the generation of the humanized mice by transferring human CD34$^+$ cells to NOG mice with transgenic expression of human GM-CSF and IL-3. These mice were administered with Ctrl or a humanized anti-CD300A mAb (TNAX103) 2 h before biIRI. (**E**) Flow cytometric analysis of CD300A expression on human and mouse CD45$^+$ cells in the kidney in the humanized mice after biIRI. (**F** and **G**) Plasma NGAL (F) and BUN and Cre (G) before (0) and 48 h after biIRI in the humanized mice that had been i.v. injected with TNAX103 mAb or Ctrl (n = 5 or 6, respectively). Means ± SEM and pooled from 2 (F and G) and 3 (C) experiments. Student's *t*-test (C) and two-way ANOVA (F and G). *, $P < 0.05$; **, $P < 0.01$; ***, $P < 0.001$; ****, $P < 0.0001$.